

MOLECULAR AND ATOMIC EXCITATION STRATIFICATION IN THE OUTFLOW OF THE PLANETARY NEBULA M27

STEPHAN R. McCANDLISS,¹ KEVIN FRANCE,² ROXANA E. LUPU,¹ ERIC B. BURGH,³ KENNETH SEMBACH,⁴
JEFFREY KRUK,¹ B-G ANDERSSON,¹ AND PAUL D. FELDMAN¹

Received 2006 November 10; accepted 2007 January 5

ABSTRACT

High-resolution spectroscopy with *FUSE* and *HST* STIS of atomic and molecular velocity stratification in the nebular outflow of M27 challenge models of the abundance kinematics in planetary nebulae. The simple picture of a very high speed (~ 1000 km s⁻¹), high-ionization, radiation-driven stellar wind surrounded by a slower (~ 10 km s⁻¹) mostly molecular outflow, with low-ionization and neutral atomic species residing at the wind interaction interface, is not supported. Instead, we find vibrationally excited H₂ intermixed with mostly neutral atomic species at a transition velocity (33 km s⁻¹) between a fast (33–65 km s⁻¹) low-ionization zone and a slow (≤ 33 km s⁻¹) high-ionization zone. Ly α fluorescence of H₂ has been detected, but far-UV continuum fluorescence has not. The diffuse nebular medium is inhospitable to molecules and dust. Maintaining a modest equilibrium abundance of H₂ [$N(\text{H}_2)/N(\text{H I}) \ll 1$] in the diffuse nebular medium requires a source of H₂, mostly likely the clumpy nebular medium. The stellar SED shows no sign of reddening [$E(B - V) < 0.01$], but paradoxically H α /H β indicates $E(B - V) \sim 0.1$. The enhancement of H α /H β in the absence of dust may result from a two-step process of H₂ ionization by Lyman continuum photons followed by dissociative recombination [$\text{H}_2 + \gamma \rightarrow \text{H}_2^+ + e^- \rightarrow \text{H}(1s) + \text{H}(nl)$], which ultimately produces fluorescence of H α and Ly α . In the optically thin limit at the inferred radius of the velocity transition, we find that dissociation of H₂ by stellar Lyman continuum photons is an order of magnitude more efficient than spontaneous dissociation by far-UV photons. The importance of this H₂ destruction process in H II regions has been overlooked.

Subject headings: atomic processes — circumstellar matter — dust, extinction — ISM: abundances — line: identification — line: profiles — molecular processes — planetary nebulae: general — planetary nebulae: individual (NGC 6853) — plasmas — ultraviolet: ISM — ultraviolet: stars — white dwarfs

1. INTRODUCTION

M27 (NGC 6853, the Dumbbell) exhibits a bipolar morphology, often associated with molecular hydrogen (H₂) infrared emission in planetary nebulae (PNe) (Kastner et al. 1996). High-resolution spectra of the hot central star (CS), acquired with the *Far Ultraviolet Spectroscopic Explorer* (*FUSE*), have revealed an unusually rich set of narrow H₂ absorption features spanning the entire spectral bandpass, an indication that the molecule is vibrationally excited. *FUSE* carries no on-board source for wavelength calibrations and consequently M27 has been observed numerous times for this purpose, resulting in a high signal-to-noise data set (see Fig. 1 and McCandliss & Kruk 2007). The usefulness of these lines for wavelength calibration aside, we are presented with an interesting puzzle. What physical processes excite H₂ in PNe and how does it survive in this high-temperature and highly ionized environment?

At first glance it seems surprising to find H₂ in PNe at all. For a typical electron density of 300 cm⁻³ and temperature of 10,000 K, we estimate an *e*-folding lifetime ≈ 230 yr, assuming electron impact dissociation of H₂ at the rate given by Martin et al. (1998) $\gamma_{e^-} = 4.6 \times 10^{-13}$ cm³ s⁻¹. Nevertheless there is a whole class of PNe with bipolar morphology in which infrared H₂ emission is the defining characteristic (Kastner et al. 1996; Zuckerman & Gatley 1988). Zuckerman & Gatley concluded that the infrared

H₂ emission in M27 is shock excited, based on infrared (IR) spectroscopic diagnostics. This result is considered somewhat surprising because the close presence of a hot star suggests that far-UV continuum excited fluorescence of the H₂ may be important. For instance, Natta & Hollenbach (1998) calculate that continuum-pumped fluorescence processes dominate thermal processes in PNe evolutionary models at late times ≥ 5000 years.

Herald & Bianchi (2002, 2004) and Dinerstein et al. (2006) have reported excited H₂ absorption features in *FUSE* spectra of a handful of CSPNe located in the Galaxy and Large Magellanic Cloud. Dinerstein et al. (2006) and Sterling et al. (2005) have used *FUSE* to examine PNe with strong, extended H₂ IR emission. They find the detection of IR emission is no guarantee for finding excited H₂ in absorption and conclude the molecular material in these systems is clumped.

Many authors have discussed the clumped structures and dense knots observed in PNe, along with evidence for their origin and chemical composition (see O’Dell et al. 2002, 2003; Huggins et al. 2002; Bachiller et al. 2000; Cox et al. 1998; Meaburn & Lopez 1993; Reay & Atherton 1985 and references therein). These structures are isolated photodissociation regions (PDRs) immersed in H II regions, and it is natural to expect them to be reservoirs of molecular material in PNe, regardless of the mechanism that causes them to form. Capriotti (1973) studied the dynamical evolution of a radiation bounded PN and found that dense neutral globules form as the result of a gradually weakening radiation field in an outward-propagating ionization front. A Rayleigh-Taylor-like instability develops and eventually an optically thick spike of neutral material becomes separated from the front and forms a high-density globule where molecules can presumably form. The formation of H₂ at later stages, on dust

¹ Department of Physics and Astronomy, Johns Hopkins University, Baltimore, MD 21218; stephan@pha.jhu.edu.

² Canadian Institute for Theoretical Astrophysics, University of Toronto, Toronto, ON M5S 3H8, Canada.

³ Space Astronomy Laboratory, University of Wisconsin, Madison, WI 53706.

⁴ Space Telescope Science Institute, Baltimore, MD 21218.

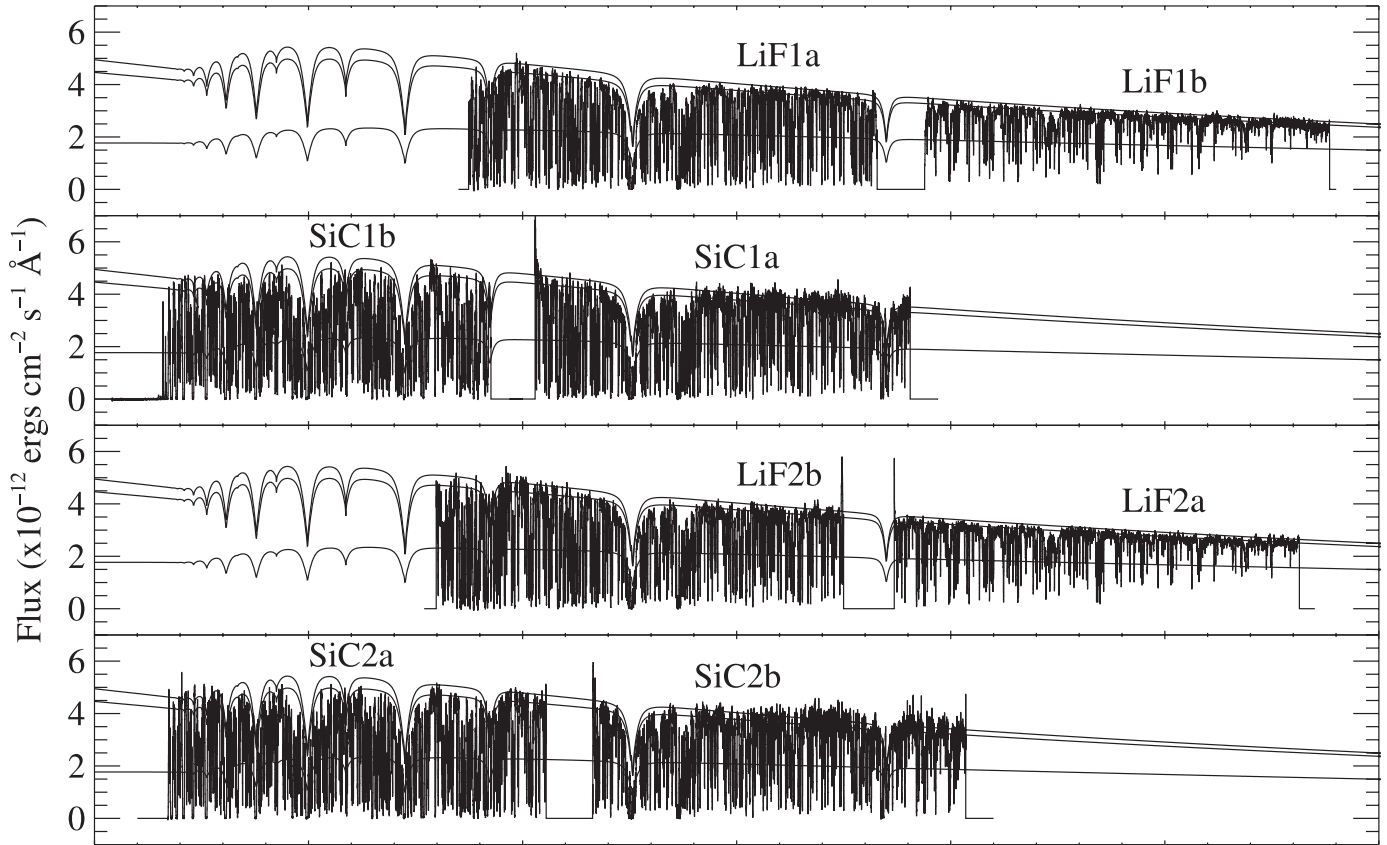


FIG. 1.— Flux of the orbital co-adds for the eight spectral segments taken through the HIRS spectrograph aperture. Individual segments are labeled. Overplotted is the model SED without extinction (*upper line*) and with $E(B - V) = 0.005$ mag (*slightly lower line*) and $E(B - V) = 0.05$ (*lowest line*) for a standard Galactic extinction curve. $E(B - V) = 0.005$ mag provides the best match to the SED in the SiC channels.

grains and in the high electron density environment via the $\text{H} + \text{H}^- \rightarrow \text{H}_2 + e^-$ reaction, has been modeled by Aleman & Gruenwald (2004) and Natta & Hollenbach (1998). Williams (1999) has discussed a shadowing instability, somewhat similar to that of Capriotti (1973), where small inhomogeneities perturb a passing supersonic ionization front, causing a corrugation that produces a large neutral density contrast farther downstream. Dyson et al. (1989) suggested molecular knots in PN are relic SiO maser spots, which originate in the atmosphere of the asymptotic giant branch (AGB) progenitor. Others have proposed that molecules may also originate from relic planetary material, either accreted and then ejected or swept up during the AGB phase preceding the formation of the nebula (see Wesson & Liu 2004; Rybicki & Denis 2001; Siess & Livio 1999; Livio & Soker 1983). Soker (1999) has discussed the signatures of surviving Uranus/Neptune-like planets in PNe.

Redman et al. (2003) have emphasized the importance of molecular observations as a means to establish the evolutionary history of the clumps, which should depend on when and where they formed during the AGB \rightarrow PN transition. The expectation is for dense clumps formed within an AGB atmosphere to have more complex molecules, due to higher dust extinction and molecular shielding, than clumps formed later in the PN phase when the stellar radiation field is harder and the overall density lower. The abundance of atomic and molecular species with respect to H_2 is of fundamental importance to assessing the predictions for the chemical evolution in PNe clumps. Observations of atomic and molecular excitation stratification in the outflow provide a fossil record of the AGB \rightarrow PN transition containing clues to the origins of the clumps.

Toward this end we explore high-resolution far-ultraviolet absorption spectroscopy, provided by *FUSE* and the Space Telescope Imaging Spectrograph (STIS) on board the *Hubble Space Telescope* (*HST*), to reveal the nebular outflow kinematics imprinted on the line profiles of a wide variety of molecular and atomic species, including H_2 , CO, H I, C I–IV, N I–III, O I, O VI, Si II–IV, P II–V, S II–IV, Ar I–II, and Fe II–III. Absorption spectroscopy samples material directly along the line of sight. We will sometimes refer to it as the diffuse nebular medium to distinguish it from the extended clumpy medium, offset from the direct line of sight, which undoubtedly differs in physical and chemical composition.

Our main objective is to quantify the H_2 excitation state, its abundance with respect to H I, and its outflow velocity with respect to other emitting and absorbing atomic and molecular species. We use this information, along with the spectral energy distribution (SED) of the CS, to constrain H_2 formation and destruction processes in the nebula.

The analysis is supported by a variety of ancillary data on M27. Long-slit far-ultraviolet spectroscopy from a JHU/NASA sounding rocket (36.136 UG) provides an upper limit to the H_2 continuum fluorescence. Long-slit optical spectrophotometry with the Double Imaging Spectrograph (DIS) at Apache Point Observatory (APO) yields the absolute flux of the CS and the surrounding nebular Balmer line emission. Dwingeloo Survey 21 cm data help constrain the velocity structure of H I. We begin by reviewing previous observations and physical properties of the nebula followed by a discussion of the various data sets. We then present the analysis, discussion, conclusions, and suggestions for future work.

2. PHYSICAL PROPERTIES AND PREVIOUS OBSERVATIONS OF M27

M27 has an elliptical shape $\approx 8' \times 5'$ as seen in visual photographs (Burnham 1978). Deep narrowband CCD imaging of $H\alpha + [N II]$ and $[O III]$ by Papamastorakis et al. (1993) has shown a faint halo of these emissions extending to $17'$. Its bipolar morphology is manifest in $H\alpha$ images as the “Dumbbell” and in the $2.12 \mu\text{m}$ image of Kastner et al. (1996) as a clumpy “bow tie” aligned with the semiminor axis. The ends of the bow tie are $\approx 3'$ wide, the waist $\approx 1'$, and the length $\approx 6'$ (see Kastner et al. 1996; Zuckerman & Gatley 1988).

Napiwotzki (1999) determined the DAO CS parameters from NLTE model atmosphere analysis and evolutionary considerations [$T = 108,600 \pm 6800$ K, $\log g = 6.7 \pm 0.23$, $\log(\text{He}/\text{H})$ by number of -1.12 dex, and $M_* = 0.56 \pm 0.01 M_\odot$]. Astrometric observations of the CS by Benedict et al. (2003) produced a distance of $d = 417^{+49}_{-65}$ pc. At this distance the $\approx 8' \times 5'$ ellipse is $1 \text{ pc} \times 0.6 \text{ pc}$ and the $1025''$ diameter of the halo is 2.1 pc . Benedict et al. give other physical parameters as well, $V = 13.98 \pm 0.03$, a total extinction $A_V = 0.3 \pm 0.06$, and a stellar radius $R_* = 0.055 \pm 0.02 R_\odot$. They find a bolometric magnitude $M_{\text{bol}}^* = -1.67 \pm 0.37$, which yields a luminosity for the CS of $L_* = 366 L_\odot$. The radial velocity of the CS in the heliocentric system was determined by Wilson (1953) to be $V_{\text{sys}} = -42 \pm 6 \text{ km s}^{-1}$.

Barker (1984) has reported on the analysis of line emission from the nebula as derived from both ground-based and *International Ultraviolet Explorer (IUE)* spectra. The emission is typical of an H II region with an electron temperature of $\approx 10,000$ K, an electron density of $\approx 300 \pm 100 \text{ cm}^{-3}$, and an elevated metallicity with respect to solar in CNO. These parameters agree well with those found by Hawley & Miller (1978) in a similar ground-based study of the nebula. Barker (1984) adopts a line-reddening parameter of $c = 0.17$ (c is defined in § 4.2.1). The literature reveals a range of nebular line-reddening parameters, $0.03 \leq c \leq 0.18$ (see Miller 1973; Kaler 1976; Cahn 1976; Barker 1984; Ciardullo et al. 1999). This translates to $0.02 \leq E(B - V) \leq 0.12$ [using $c/E(B - V) = 1.5$; Ciardullo et al. 1999, Fig. 4]. Pottasch et al. (1977) derived $E(B - V) = 0.10 \pm 0.04$ by removing a small (some would say imperceptible) 2175 \AA bump from an *IUE* spectrum. This value is nearly the same as that given by Harris et al. (1997) and Benedict et al. (2003) based on trigonometric distance determinations and absolute visual magnitude considerations. Cahn et al. (1992) report $c_r = 0.04$ derived from the ratio of 5 GHz radio flux density to $H\beta$ absolute flux.

Velocity and position resolved emission-line spectroscopy by Goudis et al. (1978) showed faint $[O I]$ and $[N II]$ profiles (beam size of $83''$) taken near the CS to be double-peaked symmetrically around the radial velocity of the system. In the outer regions the profiles converged to single peaks at the systemic velocity. The bright $[O III]$ lines (beam size of $30''$) showed similar behavior but with a lower double-peaked splitting. These observations are consistent with the presence of two nested shells expanding with projected velocities of ≈ 33 and 15 km s^{-1} , respectively. Meaburn et al. (1992) used a fiber optic image dissector fed into an echelle spectrograph to closely examine the $O III$ velocity structure in the immediate vicinity of the CS ($\approx 36''$ north-south) and found quadruple-peaked line profiles consistent with gas expanding at velocities of 31 and 12 km s^{-1} . Meaburn (2005) showed that $H\alpha$ exhibits a filled-in asymmetric profile with a half-width at half-maximum of $\approx 37 \text{ km s}^{-1}$, in contrast to the double-peaked emission exhibited by $[N II] \lambda 6584$ in the vicinity of the CS. $He II \lambda 6560$ shows a much narrower profile and is consistent with turbulent broadening alone. Examples of the $[N II] \lambda 6584$ and $H\alpha$

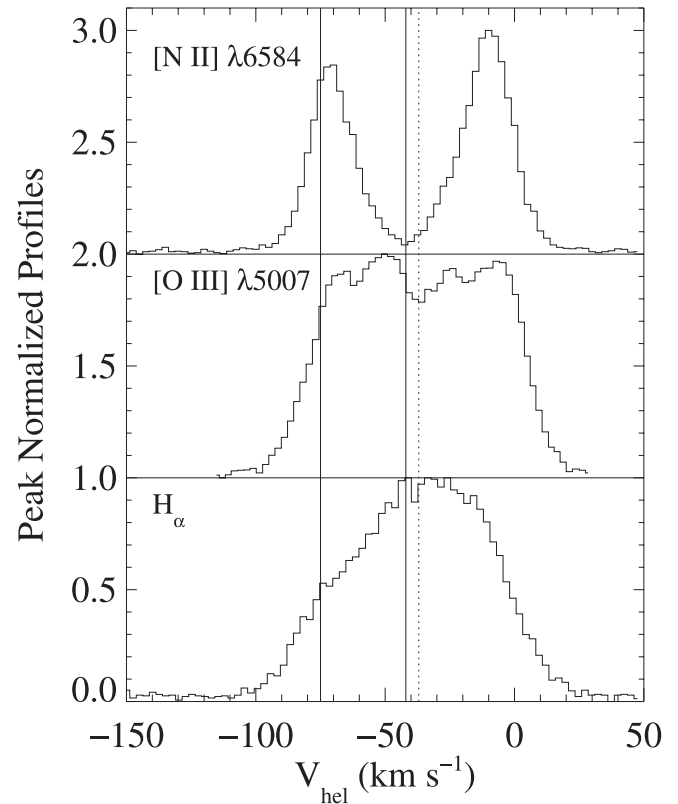


FIG. 2.—Normalized intensity profiles of $H\alpha$, $[O III] \lambda 5007$, and $[N II] \lambda 6584$ as a function of velocity. $H\alpha$ and $[N II] \lambda 6584$ were digitized from Meaburn (2005), and $[O III] \lambda 5007$ was digitized from Meaburn et al. (1992).

profiles from Meaburn (2005, Fig. 3) are reproduced in the top and bottom panels of Figure 2. The middle panel of Figure 2 shows $O III \lambda 5007$ taken from Meaburn et al. (1992, Fig. 6d). Note the base of these emission features extends to $\approx \pm 60 \text{ km s}^{-1}$.

Observations by Huggins et al. (1996) of the $CO(2-1) 230$ GHz emission lines at a position $68''$ west and $63''$ south from the CS also exhibit similar double-peaked line profiles, with a total separation $\approx 30 \text{ km s}^{-1}$. At this position they estimate a CO column density of $6.9 \times 10^{15} \text{ cm}^{-2}$ (assuming LTE with $5 \text{ K} < T_{\text{ex}} < 150 \text{ K}$). At a position $10''$ due west of the CS, Bachiller et al. (2000) show lines split by $53 \pm 1 \text{ km s}^{-1}$ (their Fig. 4), yielding an expansion velocity of $\approx 27 \text{ km s}^{-1}$ with symmetry about a heliocentric velocity of -43 km s^{-1} (at M27, $V_{\text{hel}} = V_{\text{lsr}} - 17.8 \text{ km s}^{-1}$), in good agreement with the Wilson systemic velocity. They present a map of the region (beam size $12''$), showing the CO emission to be clumpy and more or less coincident with the molecular hydrogen infrared emission observed by Kastner et al. (1996). Bachiller et al. (2000) present a picture of an ionized central region with an electron density of about $n_e \sim 100 \text{ cm}^{-3}$ surrounded by a ring of molecular clumps with densities $\sim 10^4 \text{ cm}^{-3}$ undergoing photodissociation. They suggest the clumps are similar to the “cometary” shaped features observed in great detail in the Helix Nebula (see O’Dell et al. 2002; Huggins et al. 2002; Meixner et al. 2005), although the cometary morphology is not as prominent in the Dumbbell as it is in the Helix. Meaburn & Lopez (1993) first noted (see also *HST* images by O’Dell et al. 2002) that some clumps appear as dark knots against the very bright $O III$ emission that surrounds the central region.

McCandliss (2001) gave a preliminary analysis of molecular hydrogen absorption in the *FUSE* spectra, identifying two absorption systems, one blueward of the CS radial velocity and one

redward. The blueward component has lines originating from an excited electronic ground state ($X^1\Sigma_g^+$), with rotational levels (J'') up to 15 and vibrational levels (v'') at least as high as 3. Many lines originating from $v'' = 1$ and 2 are located longward of the ground-state band head ($v' - v'' = 0 - 0$) at 1108.12 Å, and as such are unambiguous markers of “hot” H₂. In contrast, the redward component is much “cooler,” showing no unusual excitation ($J''_{\max} \approx 4$, $v'' = 0$). It is associated with nonnebular foreground gas. Here we will refine the original analysis, which was based on LWRS data acquired under *FUSE* PI team program P104.

Lastly we note that Ly α fluorescence of H₂ has recently been found in the PNe M27 and NGC 3132 by Lupu et al. (2006). The fluorescence is a direct consequence of excited molecular hydrogen, as the mechanism requires a significant population in the $v'' = 2$ levels in the presence of strong Ly α emission. J. E. Herald reports (2006, private communication) that *FUSE* observations of the CS of NGC 3132 also exhibit excited H₂ absorption lines with a roughly thermal rovibrational distribution of ≈ 1750 K.

3. DATA SETS

3.1. *FUSE*

A description of the data set and processing procedures for the *FUSE* spectra of the CS (MAST object ID GCRV12336) used in this study can be found in McCandliss & Kruk (2007). For a description of the detectors, channel alignment issues, systems nomenclature, and other aspects of the *FUSE* instrument, see Moos et al. (2000) and Sahnou et al. (2000). Briefly, the CS was observed numerous times for observatory wavelength calibration purposes. High signal-to-noise spectra, acquired in time tag mode through the high-resolution slits (HIRS) of the eight different channel segments, have been assembled. Data for each extracted channel segment consists of three 1D arrays: wavelength (Å), flux (ergs cm⁻² s⁻¹ Å⁻¹), and an estimated statistical error (in flux units). Figure 1 shows the eight individual channel segments and their spectral range for all the co-added HIRS spectra. The high density of the H₂ features is apparent.

In the low-sensitivity SiC channels the continuum signal-to-noise ratio is between 10 and 25 pixel⁻¹, while in the higher sensitivity LiF channels it is 20–55. These signal-to-noise ratios are purely statistical and do not account for systemic errors, such as detector fixed pattern noise. The resolution of the spectra changes slightly as a function of wavelength for each channel segment. In modeling the H₂ absorption (§ 4.1), we find that a Gaussian convolution kernel with a full width at half-maximum of 0.056 Å at 1000 Å (spectral resolution $R \approx 18,000$, velocity resolution $\delta V \approx 17$ km s⁻¹) provides a good match to the unresolved absorption features throughout most of the *FUSE* bandpass.

Close comparison of the wavelength registration of overlapping segments reveals isolated regions, a few Å in length, of slight spectral mismatch (\sim a fraction of a resolution element) in the wavelength solutions. Consequently, combining all the spectra into one master spectrum will result in a loss of resolution. However, treating each channel/segment individually increases the bookkeeping associated with the data analysis. Further, because fixed pattern noise tends to dominate when the signal-to-noise ratio is high, there is little additional information to be gained in analyzing a low signal-to-noise data set when high signal-to-noise is available. For these reasons we elected to form two spectra, each of which covers the 900–1190 Å bandpass contiguously, using the following procedure.

The flux and error arrays for the LiF1a and LiF1b segments were interpolated onto a common linear wavelength scale with a 0.013 Å bin, covering 900–1190 Å. The empty wavelength re-

gions, being most of the short-wavelength region from 1000 down to the 900 Å and the short gap region in between LiF1a and LiF1b, were filled in with most of SiC2a and a small portion of SiC2b, respectively. We refer to this spectrum as s12. The LiF2b, LiF2a, SiC1a, and SiC1b segments were merged similarly into a spectrum, s21. Absorption-line analyses were carried out using the composite s12 and s21 spectra (§ 4.1).⁵

3.2. *Far-UV Long-Slit Observations of M27 from JHU/NASA Sounding Rocket 36.136 UG*

JHU/NASA sounding rocket mission 36.136 UG was launched from White Sands Missile Range Launch Complex 36 on 1999 June 14 at 01:40 MST. Its purpose was to observe the hot CS of M27, provide spatial information on the excitation state of H₂ in the nebula, and investigate its dust-scattering properties. The science instrument was a 40 cm diameter Dall-Kirkham telescope with SiC overcoated Al mirrors, feeding a Rowland circle spectrograph with a 200'' \times 12'' long slit, a 900–1400 Å bandpass, and an inverse linear dispersion of ≈ 20 Å mm⁻¹. The basic configuration has been described by McCandliss et al. (1994, 2000) and Burgh et al. (2001), and two similar missions using this payload have flown (Burgh et al. 2002; France et al. 2004). This was the first flight for a newly reconfigured spectrograph with a holographically corrected concave grating (McCandliss et al. 2001), for improving the spatial resolution (3'' spacecraft pointing limited), and a high-QE KBr-coated microchannel plate with double-delay line anode (≈ 25 μm resolution element), similar to that used by McPhate et al. (1999).

The target was acquired at $\approx T + 150$ s, at which time pointing control was passed to a ground-based operator, who used a live video downlink of the nebular field to make real-time pointing maneuvers. At $\approx T + 500$ s the telescope was sealed prior to re-entering the atmosphere. The payload was recovered and post-flight calibrations were made to secure an absolute calibration.

The pointing-corrected two-dimensional spectrum is shown in the top panel of Figure 3. C II $\lambda 1335$, C III $\lambda 977$ and $\lambda 1175$, He II + N II $\lambda 1085$, N III $\lambda \lambda 989$ –991, and H I Lyman emission lines are evident along with the continuum spectrum of the CS. The bottom panel shows the extracted nebular spectrum integrated over the length of the slit, excluding the stellar continuum. The strong Ly α emission feature that fills the slit is dominated by geocoronal emission. There is a hint of H I $2s - 1s$ two-photon emission starting at Ly α and rising toward 1400 Å. The dotted blue line shows the expected brightness for a column of $N(\text{H}(2s)) = 4 \times 10^8$ cm⁻² (e.g., Nussbaumer & Schmutz 1984). There is no evidence for continuum-pumped fluorescence of H₂ or dust-scattered stellar continuum down to the detector background limit of $\approx 5 \times 10^{-17}$ ergs cm⁻² s⁻¹ Å⁻¹ arcsec⁻² indicated by the red line.

3.3. *APO DIS Long-Slit Observations of Balmer Line Ratios in M27*

It is curious that Hawley & Miller (1978) and Barker (1984) both cited problems with their H α /H β ratios being higher than the 2.9 ratio determined by Miller (1973). Hawley & Miller (1978) suggested some unidentified systematic error was affecting the ratio at the 10% level. Barker (1984) reached a similar conclusion and went so far as to decrease the H α /H β by 13% before applying an extinction correction of $c = 0.17$. Both studies find $\approx 20\%$ variations in H α /H β at different locations within the nebula.

⁵ The s12 and s21 spectra are available through the H₂ools Web site (McCandliss 2003) along with the original complete M107 data product (LWRS, MDRS and HIRS) processed by J. Kruk (2006, private communication).

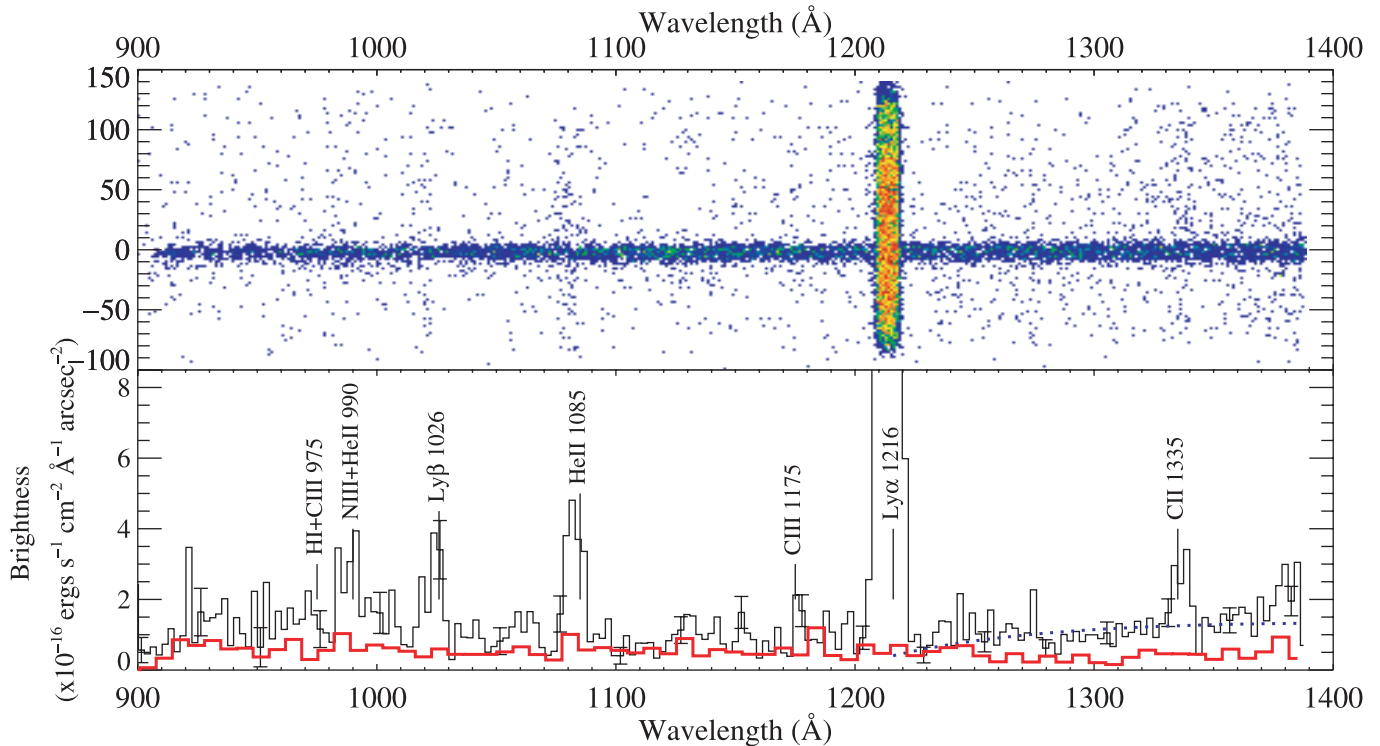


FIG. 3.— *Top*: Raw long-slit far-UV spectrum from sounding rocket experiment 36.136 UG. *Bottom*: Total nebular brightness per angstrom summed over the whole slit, excluding the continuum source. The red line is the estimated detector background. There is no significant dust scattering or H_2 continuum fluorescence emission above this background. The rise longward of $Ly\alpha$ is likely caused by $2s-1s$, two-photon emission of recombining hydrogen. The dotted blue line shows the expected brightness for a column of $N(2s) = 4 \times 10^8 \text{ cm}^{-2}$.

To more thoroughly investigate this phenomenon we recently acquired an extensive series of long-slit spectral scans of the nebula with the Double Imaging Spectrograph (DIS version III) at the ARC 3.5 m telescope at Apache Point Observatory (APO) during the nights of 2006 July 1–2 commencing at 01:15 MDT. DIS has blue and red spectra channels with back-illuminated, $13.5 \mu\text{m}$ pixel Marconi CCDs in a 1028×2048 pixel² format for recording data. The medium-resolution gratings have inverse linear dispersions of 1.85 and $2.26 \text{ \AA pixel}^{-1}$, respectively. The useful spectral ranges are $3700-5400 \text{ \AA}$ for the blue and $5300-9700 \text{ \AA}$ for the red. The plate scales are $0.42'' \text{ pixel}^{-1}$ for the blue and $0.40'' \text{ pixel}^{-1}$ for the red.

The hot subdwarf star BD +28 4211 was used as a spectrophotometric standard (Bohlin et al. 2001). This star was observed through the large $5'' \times 300''$ DIS slit for 60 s at an air mass of 1.18. The M27 CS was observed shortly thereafter for 200 s through the same aperture at an air mass of 1.02. The CS and surrounding nebula were then observed through the narrowest $0.9'' \times 300''$ DIS slit for 200 s, with the slit held fixed on the CS. The narrowest slit provides clean separation of the $[N \text{ II}] \lambda\lambda 6548, 6584$ lines from $H\alpha$. The position angle of the slit was 35° . Biases, flat fields, and emission-line spectra were recorded at twilight, and the data were reduced using custom IDL code. The CS absolute flux is shown in Figure 4 and will be discussed in § 4.2. The Balmer line long-slit profiles centered on the CS, and ratioed to $H\beta$, are shown in Figure 5 and will be discussed in § 4.2.1. Analysis of the full data set from the APO run will be presented elsewhere.

3.4. Dwingeloo H I 21 cm Observation of M27

The shapes of atomic hydrogen absorption profiles are complex, as they result from ensembles of intervening ISM absorp-

tion systems, separated in velocity space along the line of sight. Determining the column density and Doppler parameter for individual velocity components within these broad damped and saturated absorption profiles is difficult without a priori information of the line-of-sight velocity structures. One way to gain this information is to examine H I 21 cm emission data such as found in the Atlas of Galactic Neutral Hydrogen (Hartmann & Burton 1997; also known as the Dwingeloo survey). The high spectral resolution of the data is excellent for locating velocity components, provides an upper limit to the amount of neutral hydrogen in the foreground, and serves as a starting point for absorption-line modeling. The atlas, in Galactic coordinates (l, b) with $(0.5'')^2$ cells, has a velocity spacing of 1.03 km s^{-1} . The positions cover most of the sky, and the velocity coverage spans $-450 \text{ km s}^{-1} \leq v_{\text{lsr}} \leq 400 \text{ km s}^{-1}$ in local-standard-of-rest coordinates. The intensity is given in antenna temperature per velocity [$\text{K} (\text{km s}^{-1})^{-1}$] but can be converted to a H I column density, under the assumption of optically thin emission, by multiplying with a conversion factor ($0.182 \times 10^{-19} \text{ cm}^{-2}$; Hartmann & Burton 1997).

The Galactic coordinates of M27 are $l = 60.84^\circ, b = -3.70^\circ$. The neutral portion of the nebula should be at least as large as the $H\alpha$ halo detected by Papamastorakis et al. (1993) ($\geq 0.28''$), and since the Dwingeloo half-power beam width is slightly larger than the atlas grid, it is reasonable to expect some signal from the nebula to appear in the four nearest neighbor points, i.e., atlas coordinates ($l = 61^\circ, b = -3.5^\circ$), ($l = 60.5^\circ, b = -3.5^\circ$), ($l = 61^\circ, b = -4^\circ$), and ($l = 60.5^\circ, b = -4^\circ$). The column density profiles of H I as a function of velocity for these four grid points, in heliocentric velocity coordinates, are shown in Figure 6.

To reduce the nonlocal contributions we constructed a nearest neighbor minimum spectrum under the assumption that nonlocal

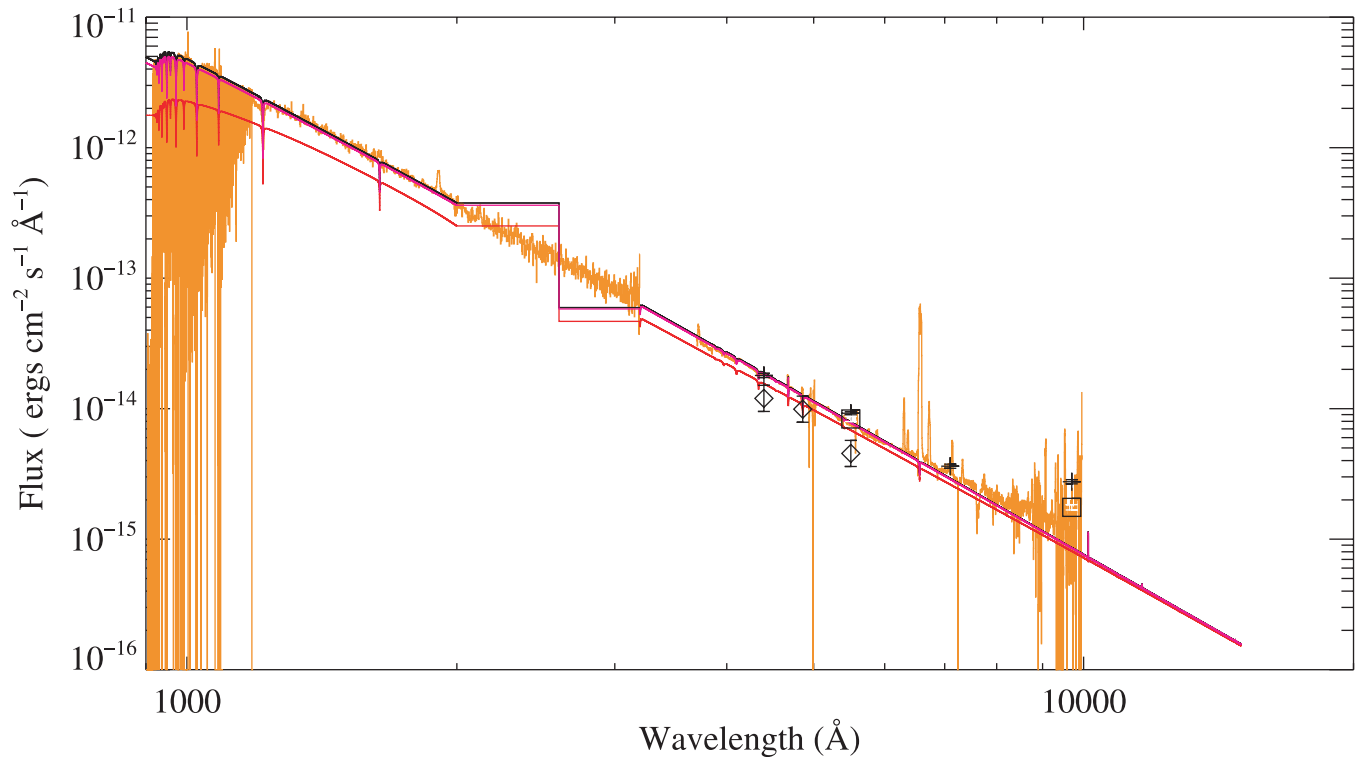


FIG. 4.—A log-log plot of the M27 central-star SED from 900 to 20000 Å, as measured by *FUSE*, *IUE*, APO, and the optical photometry of Tylanda et al. (1991; *diamonds*), Ciardullo et al. (1999; *squares*), and Benedict et al. (2003; *plus signs*). Overplotted in black, purple, and red are the respective unextinguished, lightly extinguished [$E(B - V) = 0.005$], and heavily extinguished [$E(B - V) = 0.05$] stellar continuum models. Break between 2000 and 3000 Å indicates a gap in the stellar model.

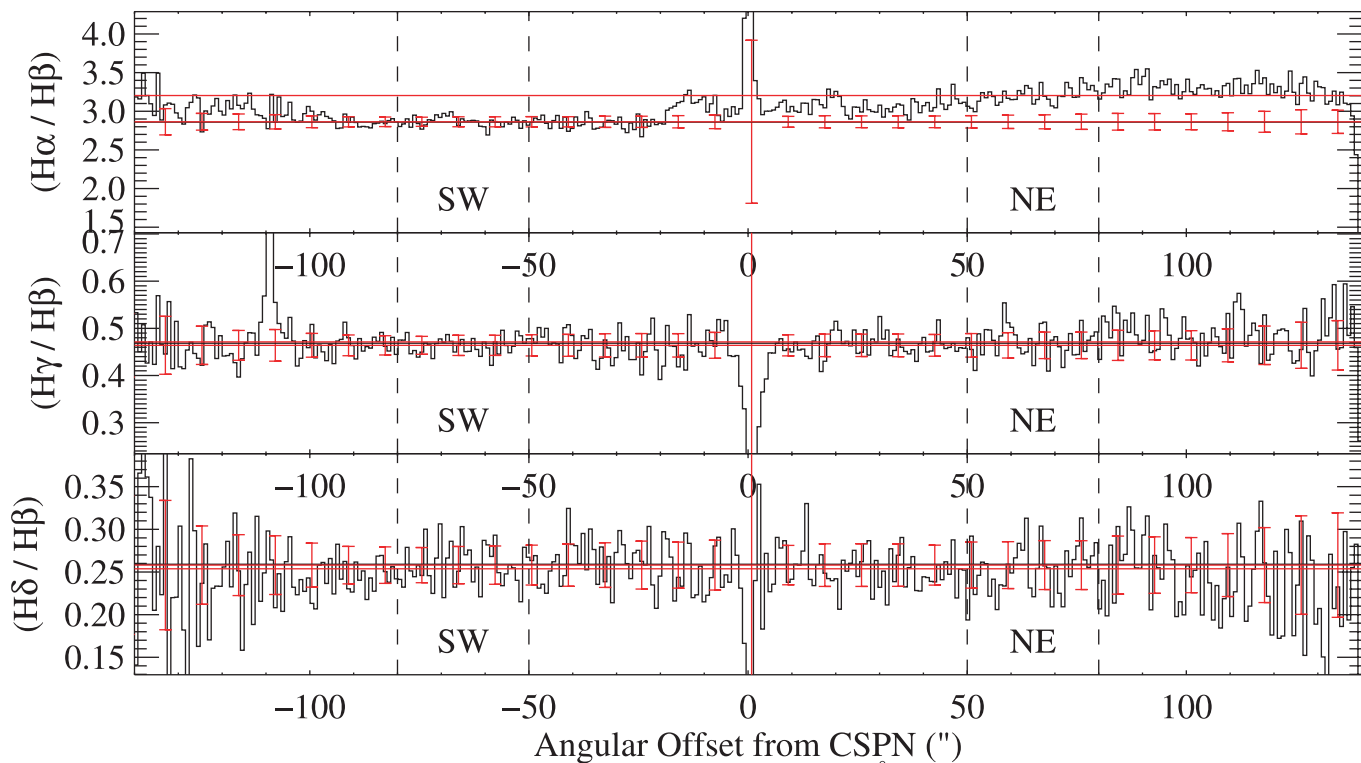


FIG. 5.—Long-slit profiles of $H\alpha/H\beta$, $H\gamma/H\beta$, and $H\delta/H\beta$. Intrinsic line ratio for a gas with a temperature of 10,000 K and a density of 100 cm^{-3} is overplotted in black. The data have been binned up by two $0.4''$ pixels. Average values in the SW and NE regions, delimited with the vertical dashed lines, are overplotted in red. Error bars are displayed with respect to the average in the SW region. All the ratios are consistent with zero extinction except for the NE $H\alpha/H\beta$ ratio. This result suggests that a mechanism other than extinction by dust is causing the $H\alpha/H\beta$ ratio to deviate from the expectations of recombination.

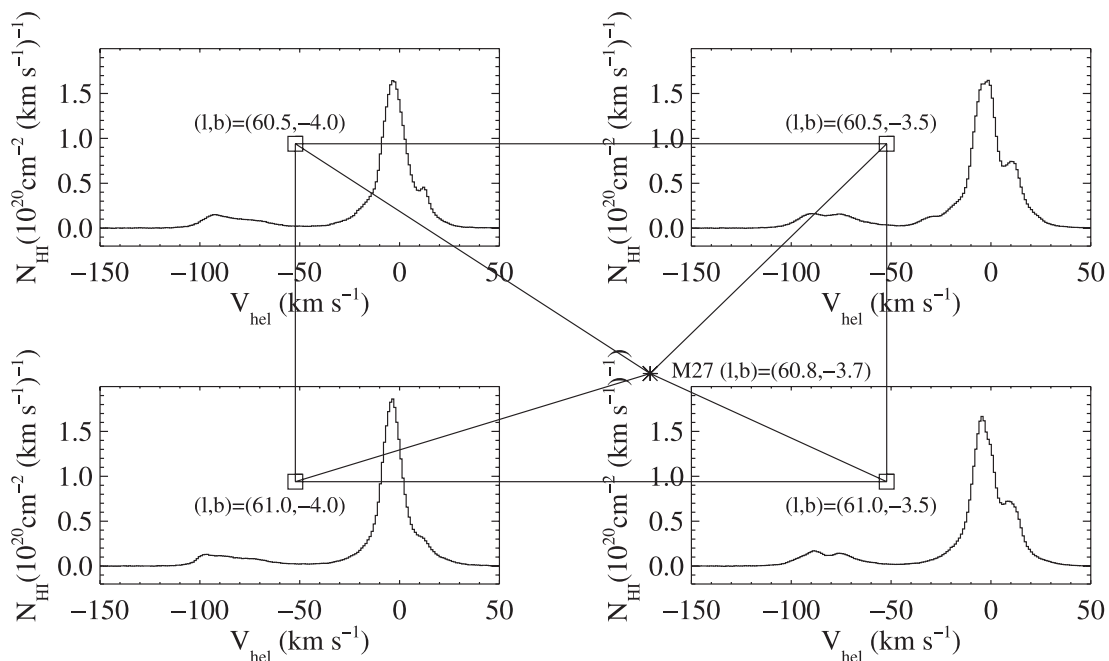


FIG. 6.—Nearest neighbor H I 21 cm emission spectra from the Dwingeloo spectral survey atlas. These spectra were used to form a minimum spectrum and a distance-weighted mean spectrum.

contributions are widespread and uniform. This assumption has been checked by examining an area out to $\pm 1.5^\circ$, which showed similar structures, typified by strong peaks near 0 km s^{-1} and smaller peaks near -85 km s^{-1} . The nearest neighbor minimum spectrum was smoothed with a five-bin boxcar average and subtracted from a similarly smoothed spectrum formed from a distance-weighted average of the same four nearest neighbors. This process is shown in Figure 7. The resulting subtraction was fit with nine Gaussian profiles spread across the range $-99 \text{ km s}^{-1} < v_{\text{hel}} < 24 \text{ km s}^{-1}$. The integrated emission column densities, rms velocity widths (b -values), and heliocentric velocities are given in columns (2), (3), and (4) of Table 1.

Column (5) shows the column densities that we adopted for the model of the Lyman series absorptions as discussed in § 4.3. Absorption-line components to the blue of the systemic velocity at -42 km s^{-1} occur within the expansion velocity inferred from the optical emission lines and can plausibly be associated with

the nebular expansion. If the absorption components to the red of -42 km s^{-1} are associated with the nebula they would have to be infalling. They are more likely to be located in the foreground.

3.5. STIS

The E140M spectrum of M27 (o64d07020_x1d.fits), taken from the Multimission Archive at the Space Telescope Science Institute (MAST), was acquired for *HST* Telescope 8638 (PI: K. Werner). These data are a high-level product consisting of the extracted one-dimensional arrays of flux, flux error, and wavelength for the individual echelle orders. The data were acquired through the $0.2'' \times 0.2''$ spectroscopic aperture for an exposure time of 2906 s and were reduced with CALSTIS version 2.18. The spectral resolution of the E140M is given in the STIS data handbook (ver. 7.0; Quijano 2003) as $R \approx 48,000$ ($\delta V = 6.25 \text{ km s}^{-1}$). The intrinsic line profile for the $0.2'' \times 0.2''$ aperture has a Gaussian core with this width, but there is non-negligible power in the wings. Comparison of the *FUSE* and STIS wavelength scales for the CS revealed a discrepant offset.

TABLE 1
H I 21 cm VELOCITY COMPONENT COLUMN DENSITIES

Component (1)	$\log N_{\text{cm}}^{\text{a}}$ [$\log(\text{cm}^{-2})$] (2)	b (km s^{-1}) (3)	V_{hel} (km s^{-1}) (4)	$\log N_{\text{abs}}^{\text{b}}$ [$\log(\text{cm}^{-2})$] (5)
1.....	19.0	2.9	-98.5	18.9
2.....	19.3	3.4	-88.7	19.0
3.....	19.6	5.3	-75.3	19.0
4.....	19.7	20.4	-75.7	18.2
5.....	19.4	5.3	-29.9	19.4
6.....	19.2	2.6	-20.0	19.2
7.....	20.3	6.2	-3.5	19.3
8.....	20.4	4.3	10.7	18.0
9.....	19.7	7.5	23.6	...

NOTE.—See Fig. 7.

^a Emission columns are upper limits. Error is ± 0.15 dex.

^b Absorption columns used in H I model.

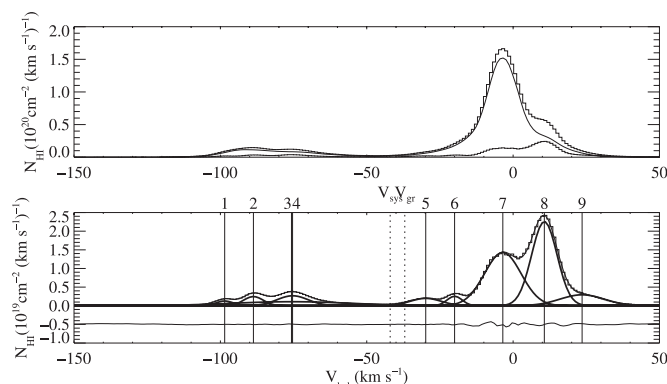


FIG. 7.—*Top*: Minimum spectrum is subtracted from the angular distance weighted mean spectrum to remove wide-angle background emission. Vertical axis is column density per km s^{-1} . Horizontal axis is heliocentric velocity. *Bottom*: Resulting spectrum contains both foreground and some background emission. Nine-component Gaussian fit is shown along with the fit residuals (offset by $-5 \times 10^{18} \text{ cm}^{-2}$). See Table 1 for total columns, velocity centroids, and Doppler parameters derived from Gaussian fits.

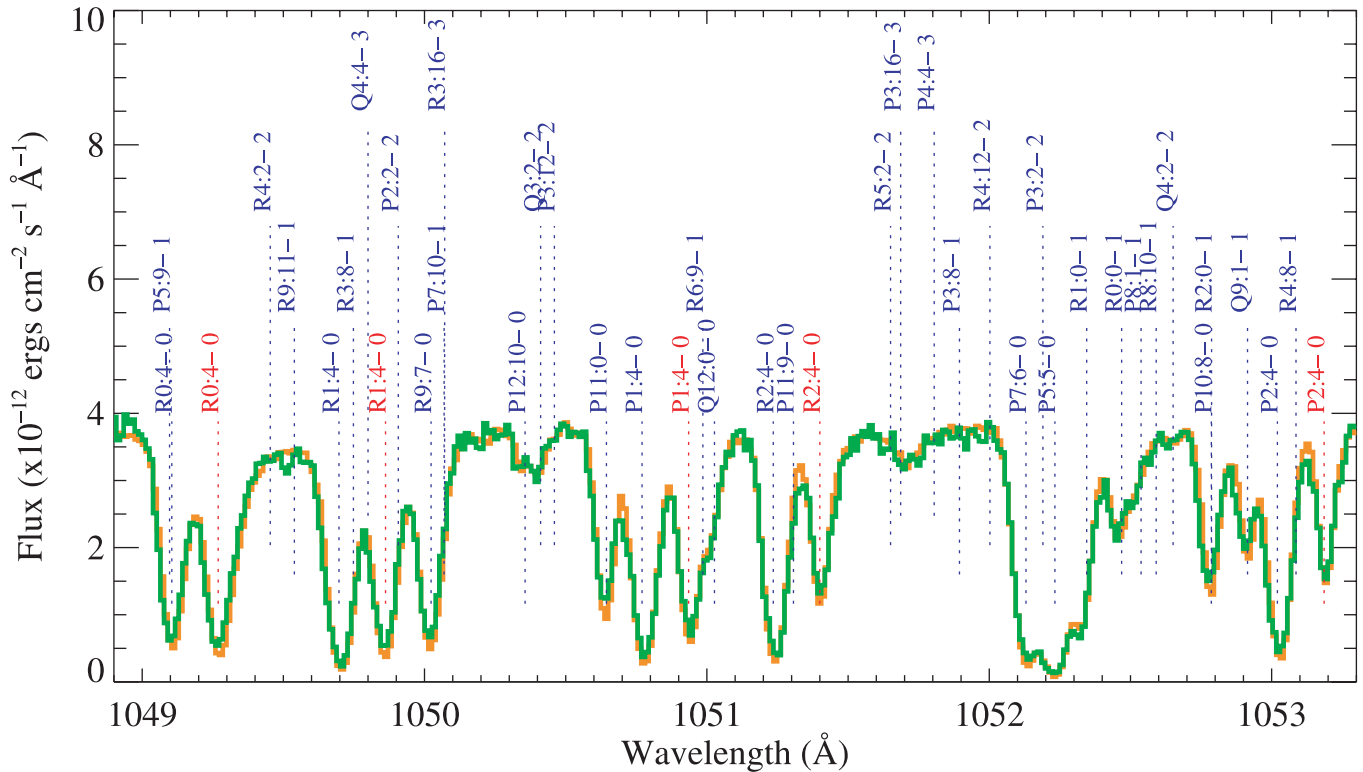


Fig. 8.—Region near the $H_2(4-0)$ band identifying the high-excitation velocity component at -33 km s^{-1} (blue) and the low-excitation component at $+14 \text{ km s}^{-1}$ (red) as measured in the CS rest frame. *FUSE* s12 and s21 spectra are overplotted in orange and green, respectively.

The establishment of a self-consistent wavelength scale is discussed in § 4.5.

4. DATA ANALYSIS

Our primary purpose is to quantify the excitation state of the H_2 in the diffuse nebular medium. The column densities of the individual rovibrational states were determined using curve-of-growth analysis. We detect essentially imperceptible reddening of the stellar SED over a decade of wavelength coverage, in contrast to the reddening determinations using the Balmer decrement method as reported in the literature (§ 2). We show new high-precision long-slit Balmer decrement ratios ($H\alpha/H\beta$, $H\gamma/H\beta$, and $H\delta/H\beta$) where $H\alpha/H\beta$ appears to be reddened in certain regions of the nebula, but the higher order decrements appear unreddened everywhere. A potential resolution of the reddening conundrum will be discussed in § 5.4.

We also produce an estimate of the total atomic hydrogen column density in the nebula to enable a discussion of H_2 formation and destruction processes. An upper limit is placed on the column density of CO in the diffuse medium, and an analysis of the excitation of C I fine-structure lines will provide a diagnostic of nebular pressure and insight into the H_2 excitation mechanism. Absorption-line profiles of high- and low-ionization species compared to the neutral profiles reveal the ionization stratification of the outflow and provide a velocity description of the nebular kinematics.

4.1. Curve of Growth for the Molecular Hydrogen Absorption Components

It seems with a first glance at Figure 1 that determining the column densities for the rovibrational transitions and identifying velocity components will be daunting. However, the regular spacing of H_2 lines arising from common rotational states, along

with the monotonic variation in transition strength with increasing upper vibrational level, makes identification of discrete velocity components straightforward. The high line density becomes an advantage, virtually guaranteeing a few lines for a given rotational state will be unblended. This allows column densities to be determined by a straightforward measurement of the equivalent widths for use in a curve-of-growth analysis.

We have identified two distinct components with heliocentric velocities of -75 and $-28 \pm 2 \text{ km s}^{-1}$. The blueward velocity component is the more highly excited, allowing the construction of curves of growth for all the rovibrational levels with $J'' \leq 11$ and $v'' \leq 1$ of the ground electronic state $X^1\Sigma_g^+$.⁶ The redward component has no extraordinary excitation, with measurable absorption only found for $J'' \leq 3$ in $v'' = 0$. Figure 8 shows a small region around the $(v'-v'') = (4-0)$ band near 1050 Å where the “blue” and “red” velocity components are identified. Blueward absorptions for $(v'-1)$, $(v'-2)$, and $(v'-3)$ in this region are also displayed.

A semi-autonomous method was developed to measure the equivalent widths of the lines, based in part on the completely autonomous method used by McCandliss (2001). All the lines for a given velocity offset and rotational state were located within a summation interval initially 13–15 pixels wide. The pixels adjacent to either side of the summation interval were used to define continuum points, through which a straight line was fit to serve as the model for the continuum in the summation region. The degree of blending was assessed interactively by plotting the spectrum surrounding each individual line in a $(-150, 50) \text{ km s}^{-1}$ interval and overplotting all the known atomic and molecular

⁶ For rotational and vibrational quantum numbers in a transition leading to an upper electronic state (e.g., either $B^1\Sigma_u^+$ or $C^1\Pi_u$) from the ground state ($X^1\Sigma_g^+$) the convention is to designate the upper state with a single prime (J', v') and the lower state with a double prime (J'', v'').

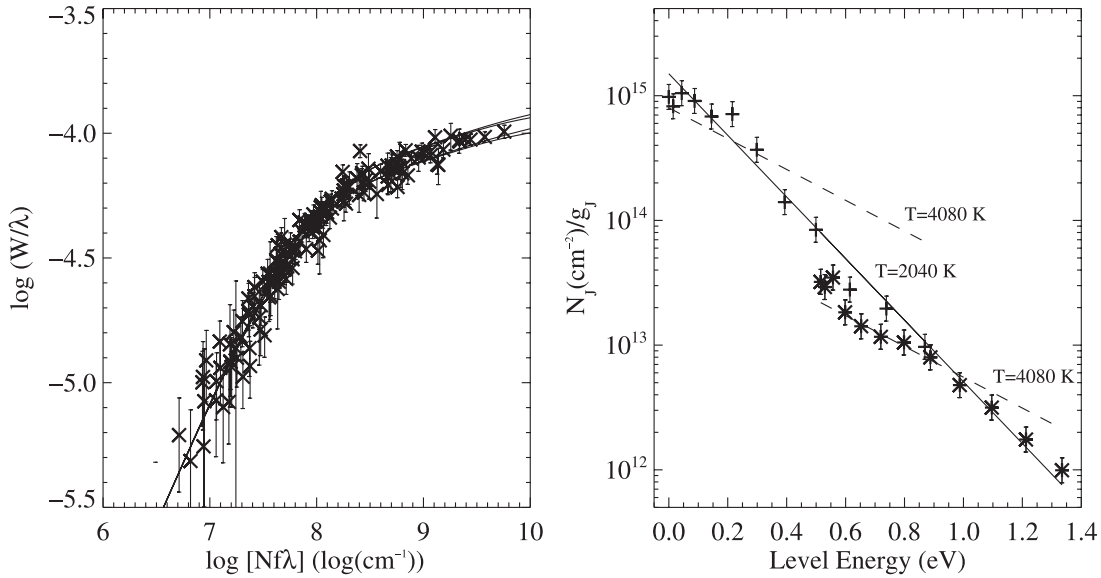


FIG. 9.—*Left*: Curves of growth for Doppler parameters of 6 and 7 km s⁻¹ along with the data. A Doppler parameter of 6.5 km s⁻¹ was adopted. *Right*: Column densities, normalized by level statistical weight, as a function of the level energy. The $v''=0$, $0 \leq J'' \leq 11$ columns are shown with plus signs, and the $v''=1$, $0 \leq J'' \leq 11$ columns are shown with asterisks. Overplotted (solid line) is a single-temperature Boltzmann distribution for $T = 2040$ K. There are statically significant deviations from the single-temperature population, although the higher $7 \leq J'' \leq 11$ states are in agreement. The lower $0 \leq J'' \leq 6$ states appear to have a flatter slope indicative of a temperature a factor of 2 higher, as the dashed lines indicate.

features. Lines with evidence of blending were rejected from the curve of growth. Examination of the lines for blends provided an opportunity to fine-tune the summation interval and continuum placement. The equivalent-width measurements were carried out on both the s12 and s21 spectra (see § 3.1), using the same summation and continuum intervals. Allowance was made for the slight local mismatches in velocity scale that exist between the s12 and s21 spectra, by locating the minimum within the integration region and adjusting the interval accordingly.

Initial curves of growth were constructed from the equivalent-width measurements using the wavelengths and oscillator strengths from Abgrall et al. (1993a, 1993b). We required at least two unblended lines for these curves. Lines from transitions with $J'' \geq 11$ and $v'' \geq 2$ are detected, but they are weak and too few to construct a reliable curve of growth. Independent χ^2 fittings were performed for each curve by varying the Doppler parameter over 2–10 km s⁻¹ and the logarithm of the column density (in cm²) over 13–18 dex. The Doppler parameters thus derived varied from 4 to 8 km s⁻¹ and the logarithmic column densities ranged over ≈ 13.5 –17 dex.

Comparing results from the s12 and s21 measurements revealed a few disagreements for the Doppler parameter (and thus column density) derived for the same rotational state. This produced an inconsistent modulation in the ortho-para ratio, expected to be $\approx 3:1$ for the odd to even rotational states. The inconsistencies were traced to curves of growth with the most saturated lines and lowest number of points. Restricting the allowed Doppler parameters in the fit to either 6 or 7 km s⁻¹ (the most common values) resolved the column density discrepancy and resulted in consistent ortho-para modulation. It also reduced the scatter when all the curves of growth for the individual rotational states from the s12 and s21 spectral measurements were combined (Fig. 9, left). The column densities for the individual rovibrational levels are listed in Table 2 along with the number of lines used for each curve of growth. The errors are dominated by placement of the continuum. Experiments were performed to gauge the effect of systematic continuum offsets on the derived

column densities. We found the column densities were consistent to within ± 0.1 in the dex for offsets within the local continuum signal-to-noise ratio.

The total column density for the hot H₂ component at -75 km s⁻¹ is $N(\text{H}_2) = (7.9 \pm 2) \times 10^{16}$ cm² with a Doppler velocity of 6.5 ± 0.5 km s⁻¹. Curve-of-growth analysis on the cold nonnebular component, for which we wish only to identify the strength of its absorption features, yielded a total column density of $(1.3 \pm 5) \times 10^{17}$ cm² with a Doppler velocity of 5 km s⁻¹. The rotational distribution is well approximated with a temperature of 200 K.

In the right panel of Figure 9 we show the population density of the rovibrational levels as a function of level energy. We use plus signs to indicate the columns for J'' in the $v'' = 0$ state and asterisks to indicate the columns for J'' in the $v'' = 1$ state. The straight solid line is the best-fit single-temperature model ($T = 2040$ K), assuming a Boltzmann distribution of level populations.

TABLE 2
DERIVED NEBULAR H₂(X¹Σ_g⁺) COLUMN DENSITIES

J''	$\log N(v'' = 0)$ [log(cm ⁻²)]	n_{COG} Lines	$\log N(v'' = 1)$ [log(cm ⁻²)]	n_{COG} Lines
0.....	15.0	2	13.6	3
1.....	15.9	11	14.4	5
2.....	15.7	8	14.2	3
3.....	16.3	4	14.6	9
4.....	15.8	4	14.1	10
5.....	16.4	8	14.6	12
6.....	15.7	8	14.1	5
7.....	15.8	5	14.5	11
8.....	15.2	7	13.9	2
9.....	15.2	11	14.3	4
10.....	14.6	13	13.5	2
11.....	14.8	5	13.8	2

NOTES.—Systematic error = ± 0.1 dex. The Doppler parameter is 6.5 ± 0.5 km s⁻¹.

TABLE 3
EXTINCTIONS DERIVED FROM BALMER RATIOS

RATIO	$f(\lambda)^a$	INTRINSIC RATIO ^b	OBSERVED RATIO		$E(B - V)$	
			SW ^c	NE ^c	SW	NE
H α /H β	-0.33	2.859	2.868 \pm 0.041	3.205 \pm 0.066	0.003 \pm 0.013	0.100 \pm 0.018
H γ /H β	0.15	0.4685	0.4627 \pm 0.0093	0.4724 \pm 0.0144	0.024 \pm 0.039	-0.016 \pm 0.059
H δ /H β	0.20	0.2591	0.2585 \pm 0.0075	0.2508 \pm 0.0082	0.003 \pm 0.042	0.047 \pm 0.048

NOTE.—Data rebinned by 16 pixels.

^a From Barker (1984).

^b Intrinsic line ratios from Brocklehurst (1971).

^c SW values are averaged over ($-80''$, $-50''$), the NE over ($50''$, $80''$); see dashed lines in Fig. 5.

This model is not successful, as there are statistically significant deviations from a single-temperature Boltzmann distribution.

The variation of population density as a function of level energy is quite different from what is usually observed in the cold ISM. Typically the first two rotational levels are consistent with a rather steep slope with a temperature $T_{01} \sim 80$ K, while the higher rotational levels flatten, giving the appearance of a higher “temperature” of several hundred degrees or more (Spitzer & Cochran 1973). The excess column in the $J > 1$ levels has long been thought to be caused by far-ultraviolet continuum fluorescence, but recently Gry et al. (2002) has questioned this hypothesis. They favor a true two-temperature model for the ISM.

Regardless, here we have the opposite case. In each vibrational level $v'' = 0, 1$ the trend is for the lower rotational states to have flatter slopes (higher temperature) than the higher rotational states. Reproduction of the energy-level distribution found here will be an interesting challenge for H₂ excitation models (see Spitzer & Zweibel 1974; Black & Dalgarno 1976; Shull 1978; van Dishoeck & Black 1986; Sternberg & Dalgarno 1989; Draine & Bertoldi 1996). We note how the modeling by Spitzer & Zweibel (1974) shows qualitatively how the “curvature” of the population density can go from “concave” to “convex” as the parameters change from a low-temperature, low-density, and low-photoexcitation-rate environment to either a high-photoexcitation-rate or a high-density environment. However, they do not attempt to explore temperatures in excess of 1000 K.

4.2. Central-Star Spectral Energy Distribution and Extinction

SED models with CS parameters taken from the literature provide a fairly precise match to the stellar continuum observed by *FUSE*. This allows us to determine the line-of-sight extinction and provides a reasonable stellar continuum to use for assessing the success of our model of atomic and H₂ absorption. The combined SED and absorption model has been used by McCandliss & Kruk (2007) to identify 63 photospheric, nebular, and non-photospheric absorption features of ionized and neutral metals, lurking amid the sea of hydrogen features.

In Figure 4 we show a log-log plot of the CS SED from 900 to 20000 Å, as measured using *FUSE*, *IUE*, and the APO DIS, along with the optical photometry (Tylenda et al. 1991; Ciardullo et al. 1999; Benedict et al. 2003). Overplotted is a synthetic stellar flux interpolated from the grid of Rauch (2003) with $\log g = 6.5$, $T = 120,000$ K, and ratio of H/He = 10/3 by mass. This model includes no metals and is consistent with, although slightly hotter than, the quantitative spectroscopy of Napiwotzki (1999). It is slightly cooler than the determination of Traulsen et al. (2005). The temperature and gravity adopted for our model has slightly less pressure broadening and is a better match to the observed Lyman lines toward the series limit. We also adopt a

stellar mass of $0.56 M_{\odot}$ as suggested by post-AGB evolutionary tracks.

Use of this mass along with the above gravity required a distance of 466 pc to match the absolute flux, which is at the upper limit given by Benedict et al. (2003). Beyond our immediate need to match the absolute flux for the given gravity and mass there is no particular reason to prefer this distance over that derived by Benedict et al. Questions regarding the acceptable uncertainty in distance, absolute flux, and derived stellar parameters are best left for a stellar model specifically tailored to include the effects of metals, gravity, and evolutionary state. For our purpose, the high stellar temperature places the SED longward of the Lyman limit in the Rayleigh-Jeans regime, so the shape of the SED is insensitive to our assumptions of temperature, gravity, metallicity, mass, and distance. Consequently, long-range changes in SED shape produced by reddening can be constrained with a high degree of confidence.

The model flux is shown in Figure 4 with reddenings of $E(B - V) = 0.00, 0.005, \text{ and } 0.05$ assuming the $R_V = 3.1$ curve of Cardelli et al. (1989). An extinction of $E(B - V) = 0.05$ is clearly too high. As a convenience we adopt a very modest extinction of $E(B - V) = 0.005$, as seen most clearly in Figure 1 to make the continuum toward the Lyman edge match the stellar SED. The lack of any significant extinction is roughly consistent with the total nebular hydrogen, derived in § 4.3, and the standard conversion for color excess to total hydrogen column of $N(\text{H})/E(B - V) = 5.8 \times 10^{21} \text{ cm}^{-2} \text{ mag}^{-1}$ (Bohlin et al. 1978).

4.2.1. Balmer Line Reddening

Reddening by dust in PNe is often estimated by comparing the measured Balmer emission ratios to the intrinsic ratios produced by hydrogen recombination. The intrinsic intensity ratio (in flux units) of $I(\text{H}\alpha)/I(\text{H}\beta) \simeq 2.859$ at an electron temperature of 10^4 K and density of 10^2 cm^{-3} is accurate to within $\approx \pm 5\%$ for a wide range of the electron temperature and density ($5000 < T_e$ [K] $< 20,000$, $10^2 < N_e$ [cm^{-3}] $< 10^6$) (Brocklehurst 1971). The extinction parameter c is given in

$$I(\lambda)/I(\text{H}\beta) = F(\lambda)/F(\text{H}\beta)10^{cf(\lambda)}, \quad (1)$$

where the intrinsic ratio is $I(\lambda)/I(\text{H}\beta)$, the observed ratio is $F(\lambda)/F(\text{H}\beta)$, and $f(\lambda)$ is the line attenuation, relative to H β , at any wavelength for the given extinction curve (see Miller & Mathews 1972; Cahn 1976). The extinction parameter may be converted to selective extinction by adopting the ratio of $c/E(B - V) = 1.5$ as shown by Ciardullo et al. (1999) in their Figure 5.

Balmer emission line spatial profiles for H α , H β , H γ , and H δ in a $\pm 140''$ region to either side the CS at a position angle of 35°

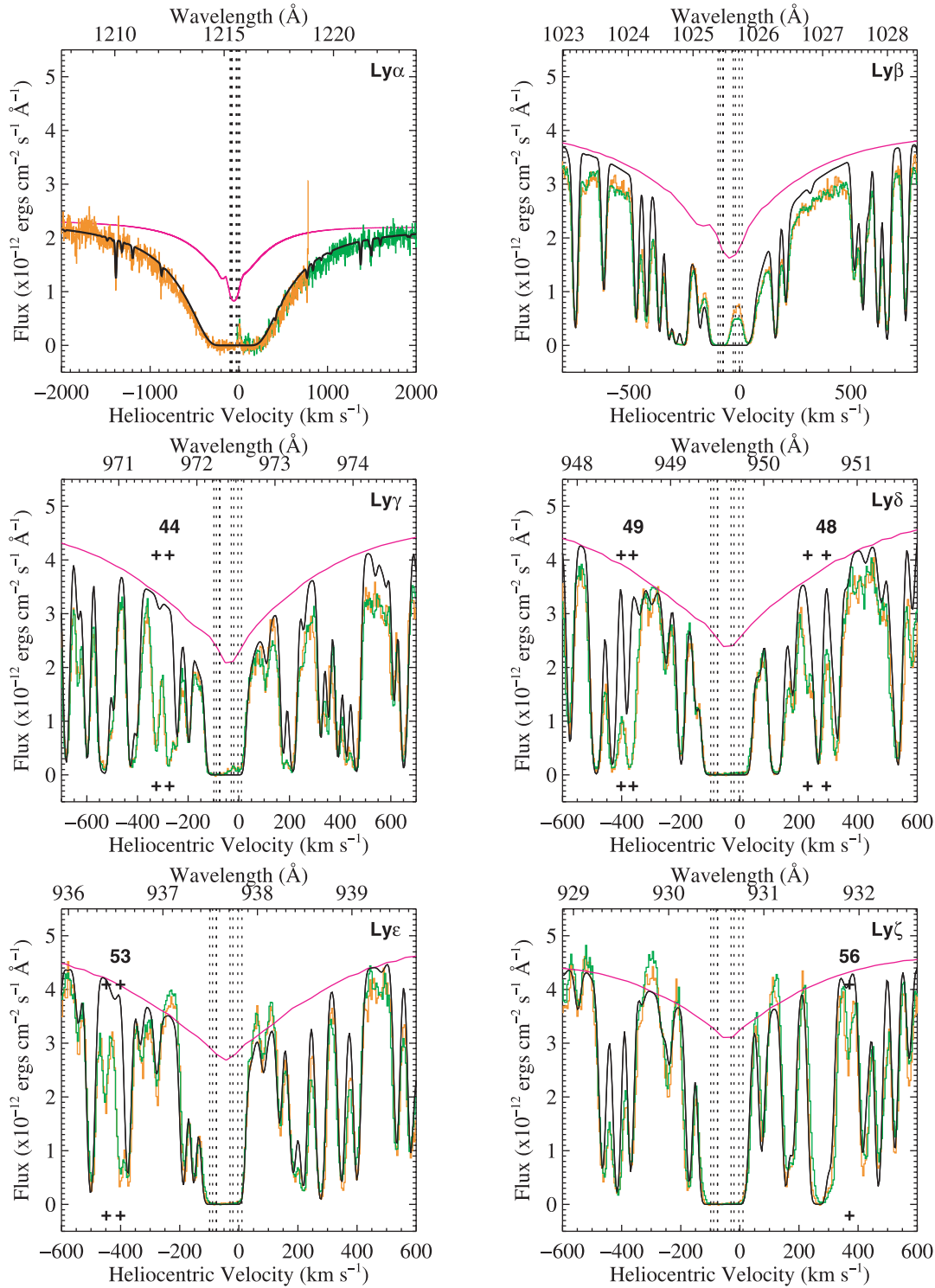


FIG. 10.—Lyman series model fits ($\text{Ly}\alpha$ – $\text{Ly}\mu$). The long-dashed lines near the center of the profiles mark the velocities of the absorption components determined from the Dwingeloo data. In $\text{Ly}\alpha$ the two STIS E140M orders are shown in orange and green. The *FUSE* data are shown as orange (s12) and green (s12). The stellar continuum is in purple and the absorption model is in black. The numbered plus signs mark absorption features tabulated in Table 2 of McCandliss & Kruk (2007).

were acquired as discussed in § 3.3. The line ratios, with respect to $\text{H}\beta$, are displayed in Figure 5 with a 2 pixel ($0.9''$) binning. The reddenings derived from these ratios (Fig. 5) are inconsistent and are summarized in Table 3. The first column specifies the line ratio, the second is the extinction multiplier taken from Barker (1984), the third is the intrinsic line ratio for a temperature of 10,000 K and a density of 100 cm^{-3} taken from Brocklehurst (1971). The fourth and fifth columns are the average line ratios

and standard deviations for the southwest and northeast regions after rebinning the data by 16 pixels ($7.2''$), and the sixth and seventh columns are the derived selective extinctions and associated errors. The northeast $\text{H}\alpha/\text{H}\beta$ ratio suggests $E(B - V) = 0.10 \pm 0.02$, while all the rest of the ratios are consistent with much lower or no extinction.

The line ratio averages in the fiducial southwest and northeast regions have standard deviations of 1.5%–3% after rebinning by

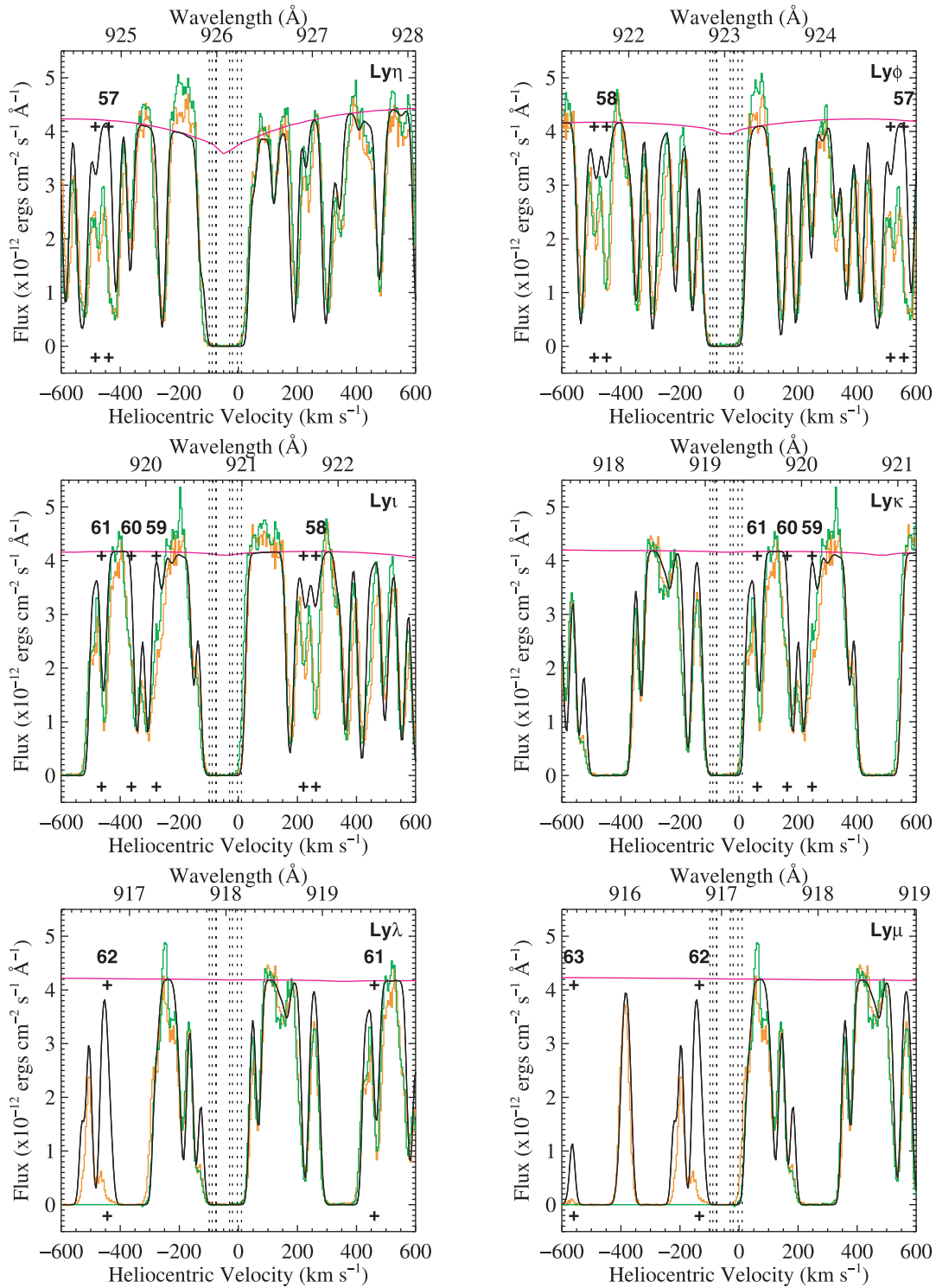


FIG. 10—Continued

16 pixels. The large error bars in the derived $E(B - V)$ serve to emphasize that Balmer line ratio determinations to a precision of better than 1% are required for $E(B - V) < 0.01$. We note that in the immediate vicinity of the star $H\alpha/H\beta = 3.03$, yielding $E(B - V) = 0.051$, which is much too large to be consistent with the observed far-ultraviolet SED (see § 4.2), assuming the line-of-sight extinction is close to the Galactic standard.

We concluded in the previous section that dust along the diffuse line of sight produces $E(B - V) \leq 0.01$ mag. Here we find the extinction in the extended medium is low to nonexistent. We

conclude that dust is not widespread, although it may be confined to the clumpy medium. The inconsistencies in Balmer reddening measures suggest that a process other than extinction by dust is contributing to $H\alpha/H\beta$ ratio excess. We will discuss this issue further in § 5.4.

4.3. Atomic Hydrogen Absorption Model

In Table 1 we list the column densities, Doppler velocities, and heliocentric velocity offsets inferred from the Dwingeloo data (§ 3.4). The 21 cm emission column densities listed in column (2)

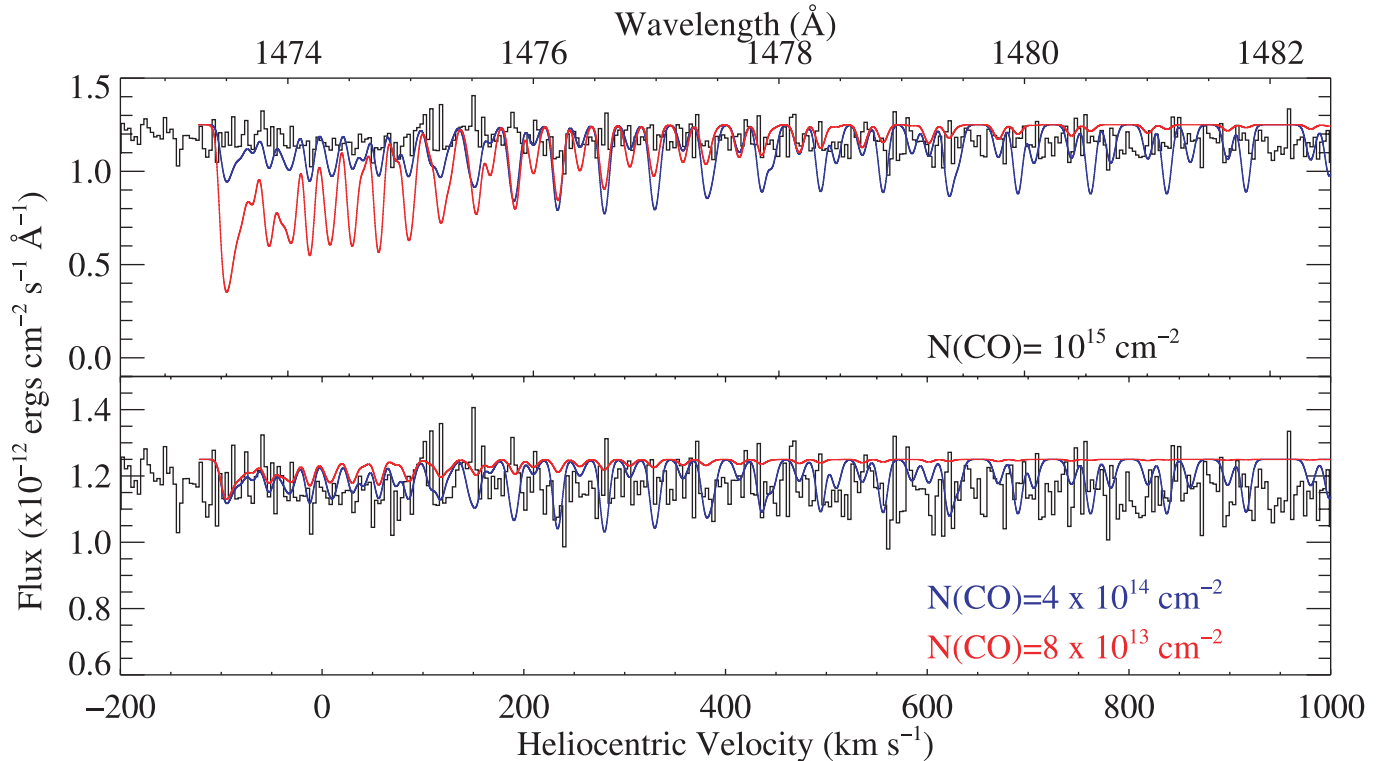


FIG. 11.—*HST* STIS E140M spectrum of the region around CO $A-X(2-0)$, the strongest band in the $A-X$ absorption series. *Top*: Two different excitation temperature models (3000 K; *blue*) and (300 K; *red*) of the $(2-0)$ band using the same column, 10^{15} cm^{-2} , as suggested from CO mm measurements. *Bottom*: Noise-bounded upper limits to the line-of-sight CO column for the two excitation temperatures. Note the scale change between the two panels. The upper limit drops for decreasing excitation temperatures, because the population becomes concentrated in the lower rotational levels as temperature decreases.

have contributions from both background and foreground emission, so they provide an upper limit to the expected foreground absorption column densities. We are mostly concerned with finding reasonable numbers for the nebular absorption, i.e., those components shortward of the stellar systemic velocity of -42 km s^{-1} , components 1–4. We will refer to components 5–9 as the nonnebular ISM components.

The adopted neutral hydrogen absorption model, the components of which are listed in column (5), was determined with the following procedure. We initially allowed the two components nearest to V_{sys} (5 and 6) to retain the maximum column suggested by the emission-line fit. The two components nicely filled the centers of the $\text{Ly}\alpha$ – $\text{Ly}\mu$ lines. We then moved to the blueward side and reduced the column of component 1 until a good agreement was found in the most saturated lines $\text{Ly}\eta$ – $\text{Ly}\mu$. We continued to add in components 2, 3, and 4, reducing the columns as necessary to smoothly match the absorption in the saturated lines. Once we were satisfied with the blue-edge fit we proceeded to the redward components. It was determined that component 9 produced too much red-edge absorption in all the Lyman series lines, and it was eliminated from further consideration. We found that only a modest amount of component 8 was necessary to match the redward edge of $\text{Ly}\alpha$. Finally component 7 was added to reduce the absorption gap between components 6 at -20 km s^{-1} and 8 at 11 km s^{-1} . Changing the column density of any one component by the error in the emission-line fit (0.15 dex) did not appreciably cause deviations of the resulting model with the data. The constraints on the formation and destruction of molecular hydrogen within the nebula, which we discuss in § 5.3, are immune to the details of the velocity distribution of H I derived from the Dwingeloo data.

Figure 10 shows an overlay of the adopted atomic and H₂ absorption model on the $\text{Ly}\alpha$ – $\text{Ly}\mu$ lines from STIS and *FUSE*. The $\text{Ly}\alpha$ profile from the STIS E140M observation spans 2 orders, plotted as orange and green. The rest of the Lyman series are from *FUSE* with the s12 spectrum shown in orange and s21 shown in green. The stellar SED is shown in purple and the model is in black. The locations of the individual H I velocity components from Table 1 are marked with vertical dotted lines. The model includes the H₂ absorption determined in § 4.1. A comparison of the hydrogen absorption model against the s12 and s21 spectra for the entire *FUSE* wavelength range, along with metallic absorption system identifications arising from the photosphere, the nebula, and nonnebular ISM, can be found in McCandliss & Kruk (2007). We see that the model continuum in the vicinity of $\text{Ly}\beta$ is $\sim 10\%$ too high, while at the shortest wavelengths it is low by a similar amount. There are also indications of absorption from O I and N II features (McCandliss & Kruk 2007, Table 2).

Although the agreement of the model with the data is excellent, the procedure adopted here for constraining the neutral hydrogen column in the nebula is not ideal and in all likelihood provides a nonunique solution. However, the result is at least plausible, well within factors of 2, given the uncertainty associated with the large background subtraction necessitated by the coarse angular resolution of the Dwingeloo data cube. A high angular resolution, 21 cm mapping of the nebula would provide a more useful constraint on the velocity components, column densities, and Doppler widths associated with the nebula. We are mainly concerned with the total H I column density of the nebula rather than the individual components. The sum of components 1–4 is $N(\text{H I})_{\text{neb}} = (3.0 \pm 1) \times 10^{19} \text{ cm}^{-2}$. The nonnebular components 5–8 total to $N(\text{H I})_{\text{non}} = (6.2 \pm 1) \times 10^{19} \text{ cm}^{-2}$.

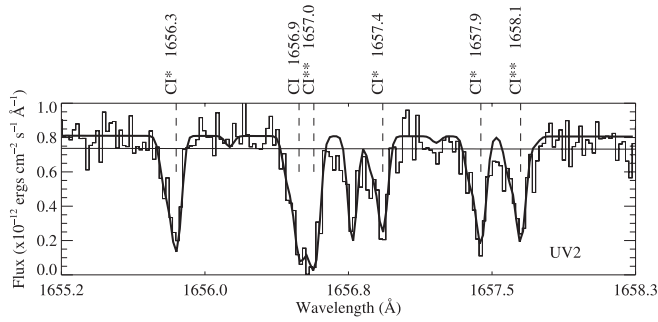


Fig. 12.—Model of the neutral carbon multiplet UV2 (smooth line) is overlaid on the observed *HST* STIS spectrum (histogram). The nebular C I, C I*, and C I** lines are labeled. The cold, nonnebular C I and C I* lines are not labeled, but the absorption is evident. There is no nonnebular C I** component. The model SED continuum is the lower smooth line. It was increased by 10% to improve the fit. The f_1 and f_2 fractions are relatively insensitive to continuum adjustments.

4.4. CO Upper Limit and the C I Pressure Diagnostic

4.4.1. CO Upper Limits

Bachiller et al. (2000) presented a detailed contour map of the CO(2–1) emission in M27. The contours fall steeply toward the CS where, using the conversion factor suggested by Huggins et al. (1996), we estimate an upper limit for the CO column of 10^{15} cm^{-2} along the line of sight. CO has a number of strong absorption bands in the far-UV, such as the numerous $A-X$ bands spread throughout the STIS E140M bandpass, and this column density would easily be detected. In Figure 11 we show the E140M spectral region surrounding the $A-X(2-0)$ 1477.565 Å band head. In the top panel we overplot CO absorption models for representative excitation temperatures of 3000 and 300 K at a column density of 10^{15} cm^{-2} in blue and red, respectively. We assumed the Doppler parameter is the same as for H₂, 6.5 km s^{-1} . Clearly the column density is much lower than 10^{15} cm^{-2} . In the bottom panel we show models for 3000 K with a column density of $4 \times 10^{14} \text{ cm}^{-2}$ and for 300 K with a column density of $8 \times 10^{13} \text{ cm}^{-2}$. The structure in the models is on the order of the noise in the observation, so we will use these values as the (excitation tempera-

ture dependent) upper limits for line-of-sight CO. Using a lower excitation temperature would yield an even lower upper limit.

4.4.2. C I Fine-Structure Pressure Diagnostic

Although CO was not detected, we do detect excited C I, C I*, and C I** multiplets in the E140M data with a velocity of -75 km s^{-1} , coincident with the velocity of the excited H₂. The level populations of the three fine-structure levels in the ground state of C I, assuming a long enough time has passed for equilibrium to be established, are a detailed balance of the de-excitation and excitation rates set by collisions of C I with other particles (the impactors: H I, He I, p , e^- , ortho-H₂, para-H₂) and the radiative decay rates of the fine-structure levels. Jenkins & Shaya (1979) present a useful diagnostic for gas pressure based on the ratios of the column densities for $N_{C I^*}$ and $N_{C I^{**}}$ relative to the total column density $N_{\text{tot}} = N_{C I} + N_{C I^*} + N_{C I^{**}}$ ($f_1 = N_{C I^*}/N_{\text{tot}}$ and $f_2 = N_{C I^{**}}/N_{\text{tot}}$). The pressure is constrained by comparing the measured values of f_1 and f_2 against theoretical loci for f_1 and f_2 at variable temperature and density.

We determined f_1 and f_2 by χ^2 fits to the absorption profiles of the C I $\lambda\lambda 1656.27\text{--}1658.12$ UV2 multiplet using the Morton (2003) oscillator strengths. The result is shown in Figure 12. We determined a Doppler parameter of $b = 4.5 \text{ km s}^{-1}$ and we find $N_{C I} = (3.0 \pm 0.5) \times 10^{13} \text{ cm}^{-2}$, $N_{C I^*} = (8.5 \pm 0.5) \times 10^{13} \text{ cm}^{-2}$, and $N_{C I^{**}} = (10.5 \pm 0.5) \times 10^{13} \text{ cm}^{-2}$, yielding $(f_1, f_2) = (0.386, 0.477) \pm 0.04$.

The theoretical loci for f_1 and f_2 depend on the mix of impactors assumed. Jenkins & Tripp (2001) discuss three extremes: case 1 where all the impactors are neutral hydrogen, case 2 where all the hydrogen is molecular, and case 3 where all the hydrogen is ionized. They find case 2 and case 1 to yield very similar loci in the (f_1, f_2) -plane. Using their code (kindly provided by E. B. Jenkins [2006], private communication) we show the results for case 1 (left) and case 3 (right) in Figure 13. The crosshairs mark the (f_1, f_2) point and the figure ranges over the ± 0.04 error limits. Plus signs mark the density at intervals of 0.1 dex. The logarithm of the pressure, in units of $\log(n_h T) = \log(P/k)$, is printed for every density point along the loci of points for each constant temperature.

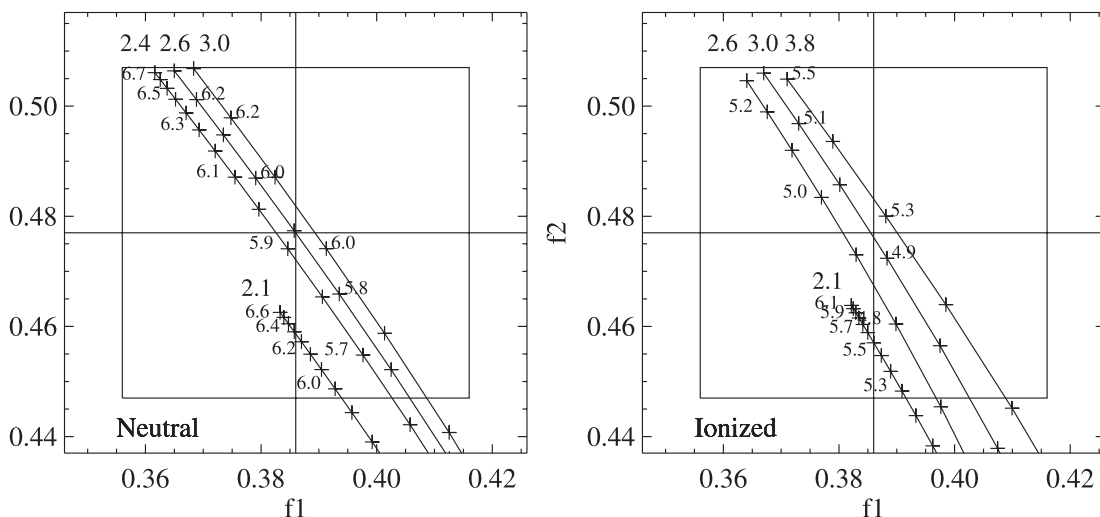


Fig. 13.—The (f_1, f_2) -planes for the expected ratios of the column densities of the C I fine-structure states, assuming neutral hydrogen impactors (left) and ionized impactors (right). The curves are the loci of (f_1, f_2) ratios for different pressures at a constant temperature. The large numbers to the upper left of each curve are the logarithms of the temperature. The logarithm of the pressure in units of $\log(n_h T) = \log(P/k)$ is printed for every other density point along the loci of points for each constant-temperature curve. The region shown is centered on $(f_1, f_2) = (0.386, 0.477)$. The box centered on this point is the error limit $(\sigma_{f_1}, \sigma_{f_2}) = (0.04, 0.04)$. Despite the large uncertainty there is nearly an order of magnitude difference in the pressure for the two limiting cases. The temperature for the ionized impactors is closer to that of H₂.

For the neutral case the $(0.386, 0.477)$ point lies on the $\log T = 2.6$ curve with a pressure of $\log(n_h T) = 5.9$, while the ionized case has $\log T \approx 3.0$ with a pressure of $4.9 < \log(n_h T) < 5.0$. The allowed range of pressure for the ± 0.04 error box in the neutral case is $5.7 \lesssim \log(n_h T) < \infty$ and for the ionized case $4.8 \lesssim \log(n_h T) < \infty$, with the ∞ density case being associated with the coldest allowable logarithmic temperature of ≈ 2.1 dex.⁷

The coincidence of the C I velocity with the H₂ velocity argues that these two species are colocated. The ~ 2000 K implied by the H₂ rovibrational distribution is closer to the temperature given by the ionized case than the neutral case. This suggests the excited C I and H₂ are located in a warm and electron-rich medium with $n_e \sim 80 \text{ cm}^{-3}$. In this environment it may be possible for H₂ to form at the interface between the ionized medium and the PDR clumps by $\text{H} + e^- \rightarrow \text{H}^- + h\nu$ followed by the $\text{H} + \text{H}^- \rightarrow \text{H}_2 + e^-$ mechanism (see Aleman & Gruenwald 2004; Natta & Hollenbach 1998). We note that our total column density for the neutral carbon, $N_{\text{C I, tot}} = 2.2 \times 10^{14} \text{ cm}^{-2}$, is ~ 2 orders of magnitude higher than what is expected for $N_{\text{C I, tot}}$ in typical H II regions, as discussed in Appendix A of Jenkins & Shaya (1979). It is likely that the source of C I in the diffuse medium is CO dissociation in the clumpy medium.

In addition to UV2, we also examined the fits for the UV3, UV4, and UV5 multiplets. We found that the χ^2 fits to these multiplets yielded slightly different results. In the cases of UV3 and UV5, there were intervening unidentified absorption features that caused the χ^2 to drift to higher columns for the $N_{\text{C I}^{*}}$ lines. In the case of UV4 the column densities were different but the $f1$ and $f2$ ratios were essentially the same. Currently there are disagreements in the literature (cf. Morton 2003; Jenkins & Tripp 2001) regarding the relative strengths of the higher multiplets with respect to UV2. Since the resulting $f1$ and $f2$ ratios all lie within the ± 0.04 error box, we decided to rely on the multiplet with the most certain oscillator strengths, UV2. Our conclusions that the C I is excited, the column density is high compared to typical H II regions, and the temperature implied by the ionized impactors is closer to that implied by the H₂ level population are unchanged by our reliance on UV2 alone.

4.5. FUSE and STIS Absorption Profiles: Ionization Stratification

The metal-line profiles show absorption from velocity components that we associate with the stellar photosphere located near the systemic velocity of the star, the blueshifted nebular outflow, and the redshifted nonnebular ISM. In general, the high-ionization species tend to appear with photospheric and nebular velocity components while the low-ionization and neutral species tend to show nebular and nonnebular components. A gravitational redshift of $\approx 5 \text{ km s}^{-1}$ can be seen in the high-excitation stellar O ve $\lambda 1371$ line. (We use the “e” specification with the atomic species designator to indicate transitions to lower levels other than the ground state).

We show a select subset of the metal-line absorption profiles in Figures 14–17. FUSE s12 and s21 spectra are shown in orange and green respectively, while the STIS lines are plotted in purple (and gray if 2 orders contain the same wavelength range). The continuum model, including the hydrogen lines, is plotted as a thin black line. The heliocentric reference frame is used. The black dashed vertical lines mark the location of the hot H₂ component at

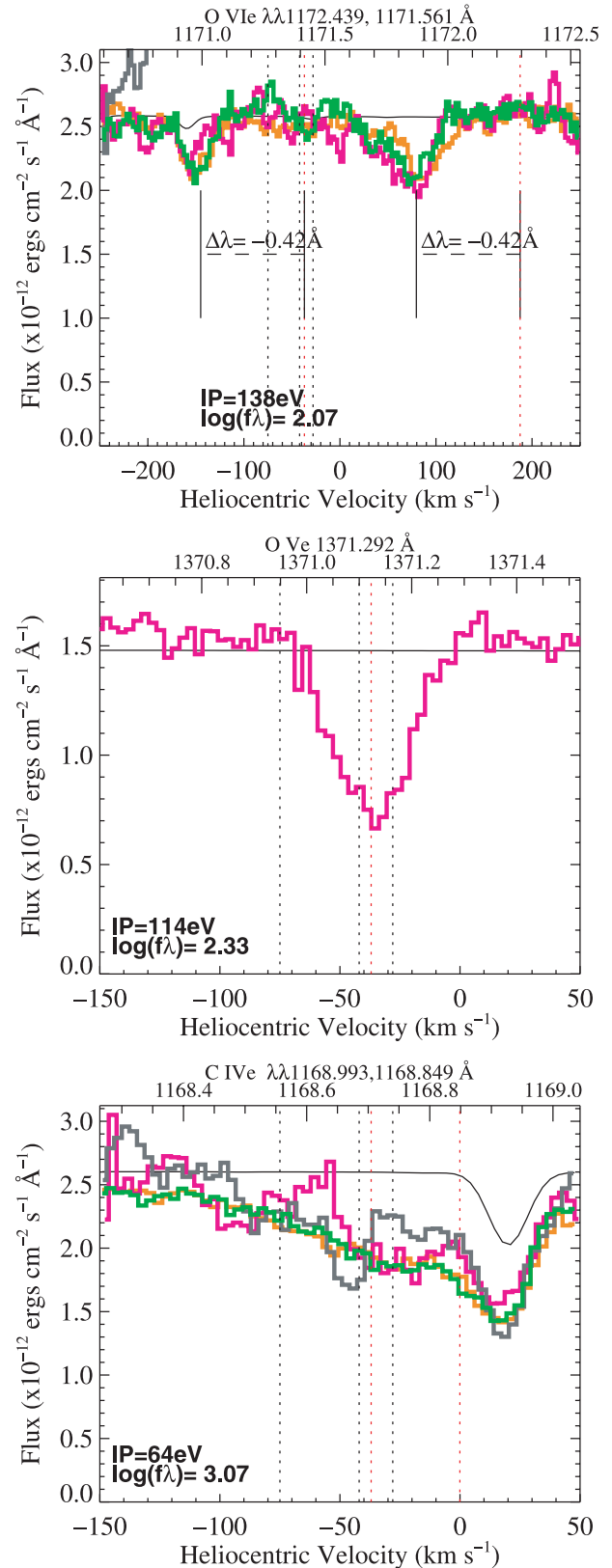


FIG. 14.—O VI*, O V*, and C IV* lines used to reconcile the FUSE and STIS wavelength offsets. O ve $\lambda 1371.292$ establishes the gravitational redshift zero point. O vie and C ive are observed by both FUSE and STIS. FUSE spectra s12 (orange) and s21 (green) and the model (black) are plotted along with overlapping STIS orders (purple and gray), if available. Vertical dashed lines mark the transition, V_{sys} , V_{gr} , and nonnebular velocities at -75 , -42 , -37 , and -28 km s^{-1} , respectively. Red lines near 0 and $+190 \text{ km s}^{-1}$ in the respective C ive and O vie panels mark the gravitational redshift of the redward doublet member. The O vie wavelength discrepancy (-0.42 \AA) from NIST is noted.

⁷ For a constant-temperature curve the $(f1, f2)$ points converge to a point as the logarithmic density approaches 6 and the diagnostic becomes less discriminatory.

–75 km s⁻¹, the systemic velocity at –42 km s⁻¹, and the cold H₂ component at –28 km s⁻¹. The red dashed vertical line marks the gravitational redshift of the systemic velocity. To convert from the nebular rest frame, subtract the heliocentric velocity from the systemic velocity.

4.5.1. Stellar Photospheric Features and the Absolute Wavelength Scale

Comparison of the *FUSE* and STIS wavelength scales revealed a systematic offset. The reconciliation of this offset is essential for investigating the kinematics of the nebular outflow, where we seek to determine the velocity of the various molecular and atomic features with respect to the systemic velocity of the nebula. Lines that arise from the photosphere should match the systemic velocity of the system less the offset caused by gravitational redshift. An absolute reference to the heliocentric velocity was established by close examination of the O ve λ 1371.296 feature, shown in the middle panel of Figure 14. This narrow line results from a transition between two highly excited states in O ve and is expected to be an excellent indicator of the photospheric rest frame (P. Chayer 2006, private communication). For a compact object of this mass and radius (§ 2) we expect the photospheric lines to experience a gravitational redshift, $V_{\text{gr}} = c[(1 - 2GM_*/R_*c^2)^{-1/2} - 1] = 5.1 \text{ km s}^{-1}$. Applying a shift of –13 km s⁻¹ to the STIS spectrum placed the centroid of the O v λ 1371.296 line at –37 km s⁻¹, as expected for a V_{sys} of –42 km s⁻¹ (Wilson 1953).

Examination of overlapping *FUSE* and STIS spectra in the wavelength regions below 1190 Å revealed some systematic disagreements. In the original analysis of the *FUSE* M27 spectra by McCandliss (2001) the hot nebular H₂ component was defined to be at –69 km s⁻¹. We found it necessary to shift the *FUSE* spectra blueward by –6 km s⁻¹, such that the hot nebular H₂ is now at –75 km s⁻¹. The most useful overlap lines for assessing the alignment were the doublet blend of C iv λ 1168.849, 1168.993 (Fig. 14, *bottom*) and the narrow O vie λ 1171.56, 1172.44 (Fig. 14, *top*). We note the wavelengths of O vie doublet given in the National Institute of Standards and Technology (NIST) online tables⁸ appear to be in error by $\approx -0.42 \text{ \AA}$ (see Jahn et al. 2007). These spectra are comparatively noisy, but the alignment with the *FUSE* spectra agrees as well as the alignment between the s12 and s21 spectra. We also used the *FUSE* N i multiplets at λ 1134–1135 and the STIS N i multiplets at λ 1200–1201, along with excited H₂ lines that appear in the STIS bandpass above 1190 Å, with the continuum plus hydrogen model of McCandliss & Kruk (2007) to assess the consistency of the wavelength reconciliation. The error in the systemic velocity (§ 2) is of order the *FUSE* resolution element and is 3 times the STIS resolution element. We consider the agreement of line profiles from spectra acquired with two different instruments to be excellent.

4.5.2. Photospheric + Nebular Features

O vi, N v, and C iv.—Figure 15 shows the high-ionization resonance doublets of O vi λ 1032.62, 1037.62, N v λ 1238.821, 1242.804, and C iv λ 1548.204, 1550.781. All these lines show photospheric absorption to the red of the systemic velocity. The strength and terminal velocity of the blueshifted portion of the line profiles increases with decreasing ionization potential. The O vi lines show only slight signs of blueshifted nebular absorption. The nebular absorption component in the N v lines is strong

only between –42 and –75 km s⁻¹, just reaching saturation at $\approx -60 \text{ km s}^{-1}$. In contrast, the nebular absorption component in the C iv lines spans –42 to –115 km s⁻¹ and is completely saturated from –50 to –95 km s⁻¹.

4.5.3. Intermediate Ionic and Neutral Nebular Absorption

C iii–ii, N iii–i, and O i.—Figure 16 shows lines of C iii–ii, N iii–i, and O i. Like the C iv lines, the C iii–ii lines are heavily saturated throughout the nebular flow region blueward of –42 km s⁻¹. The saturation makes it difficult to tell whether any one ion is dominant in the nebular outflow. N iii is strongly blended with overlapping H₂ features. However, it shows saturated absorption between –60 and –100 km s⁻¹. N ii λ 1083.994 shows absorption throughout the flow, being less saturated at low velocities and becoming completely saturated at –75 km s⁻¹. This line also shows stronger nebular absorption than nonnebular absorption. In contrast, N i λ 1200.223 shows weaker nebular absorption than nonnebular absorption. Both N i λ 1200.223 and O i show an absorption component centered on –75 km s⁻¹, which coincides with the velocity of the absorption maximum in H₂ and C i.

Si iv–ii and S iv–ii.—The transition zone between high ionization and low ionization occurs at the velocity of –75 km s⁻¹, where H i, C i, N i, O i, and H₂ show up most strongly in the nebula. The high ionization–low velocity, low ionization–high velocity dichotomy is best illustrated by examining the velocity profiles of the low-abundance metals Si and S in Figure 17. Si ii is stronger than Si iv in the zone between –75 and –110 km s⁻¹, while Si iv is stronger than Si ii in the zone between –42 and –75 km s⁻¹. The Si iii λ 1206.500 line is saturated throughout most of the flow. The S iv–S ii ions show similar behavior.

5. DISCUSSION

Here we enumerate the main findings from the analysis.

1. The nebular H₂ is highly excited with a ground state ro-vibration population that deviates significantly from the best-fit single-temperature Boltzman distribution of 2040 K. The total column density is $7.9 \times 10^{16} \text{ cm}^{-2}$. The deviations are characterized by a flatter slope for the lower rotational levels ($0 \leq J'' \leq 5$) than for the higher rotational levels ($6 \leq J'' \leq 11$).

2. Continuum fluorescence of H₂ has not been detected to the background limit of the sounding rocket observation, $\approx 5 \times 10^{-17} \text{ ergs cm}^{-2} \text{ s}^{-1} \text{ \AA}^{-1} \text{ arcsec}^{-2}$. However, Ly α fluorescence has been detected by Lupu et al. (2006). This emission mechanism is possible only for H₂ with a significant population in the $v'' = 2$ vibrational state in the presence of a strong Ly α radiation field.

3. The stellar SED exhibits negligible stellar reddening along the line of sight. This finding is at odds with the variable reddening indicated by the ratio of H α /H β intensity as reported in the literature and confirmed in this study in the immediate vicinity of the star. We note that the reddening determined by H γ /H β and H δ /H β is consistent with zero and conclude it is possible that another physical process, aside from reddening by dust, is causing the discrepant H α /H β .

4. The nebular H₂ appears at a heliocentric velocity of –75 km s⁻¹, corresponding to an expansion velocity of 33 km s⁻¹ in the nebular rest frame. H i, C i, N i, and O i exhibit strong resonance-line absorption at the same expansion velocity. The molecules and neutrals demarcate a transition velocity between a regime of high ionization and low expansion velocity ($10 \text{ km s}^{-1} \lesssim v_{\text{high}} \lesssim 33 \text{ km s}^{-1}$) and a regime of low ionization and high velocity ($33 \text{ km s}^{-1} \lesssim v_{\text{low}} \lesssim 65 \text{ km s}^{-1}$). The upper limit to the terminal expansion velocity is $\approx 70 \text{ km s}^{-1}$. These observations,

⁸ Available at http://physics.nist.gov/PhysRefData/ASD/lines_form.html.

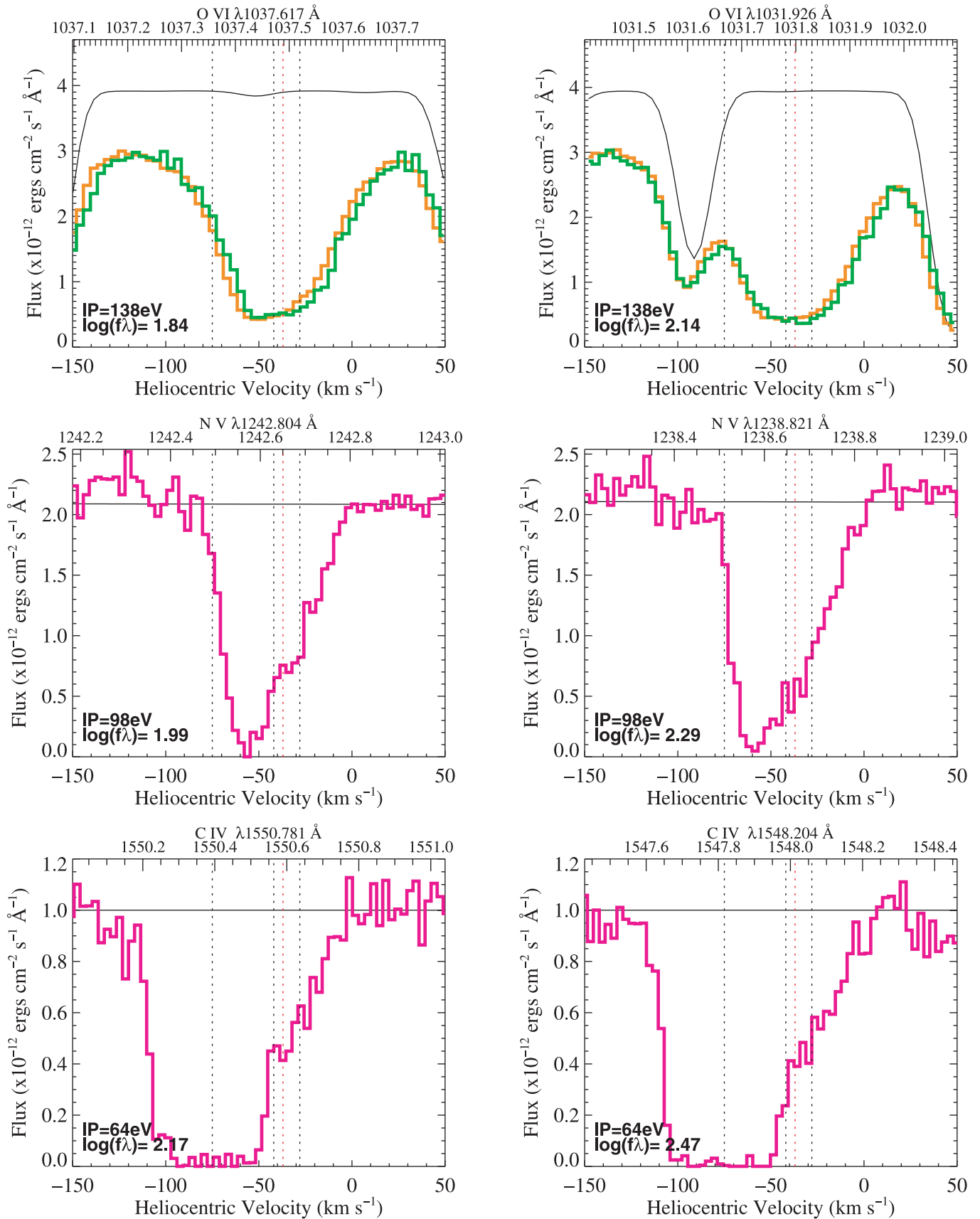


FIG. 15.— Absorption as a function of velocity for the high-ionization resonance lines of O VI, N V, and C IV, showing varying degrees of photospheric broadening to the red. Nebular outflow to the blue of systemic increases with decreasing ionization potential. See Fig. 14 for a description of the colors.

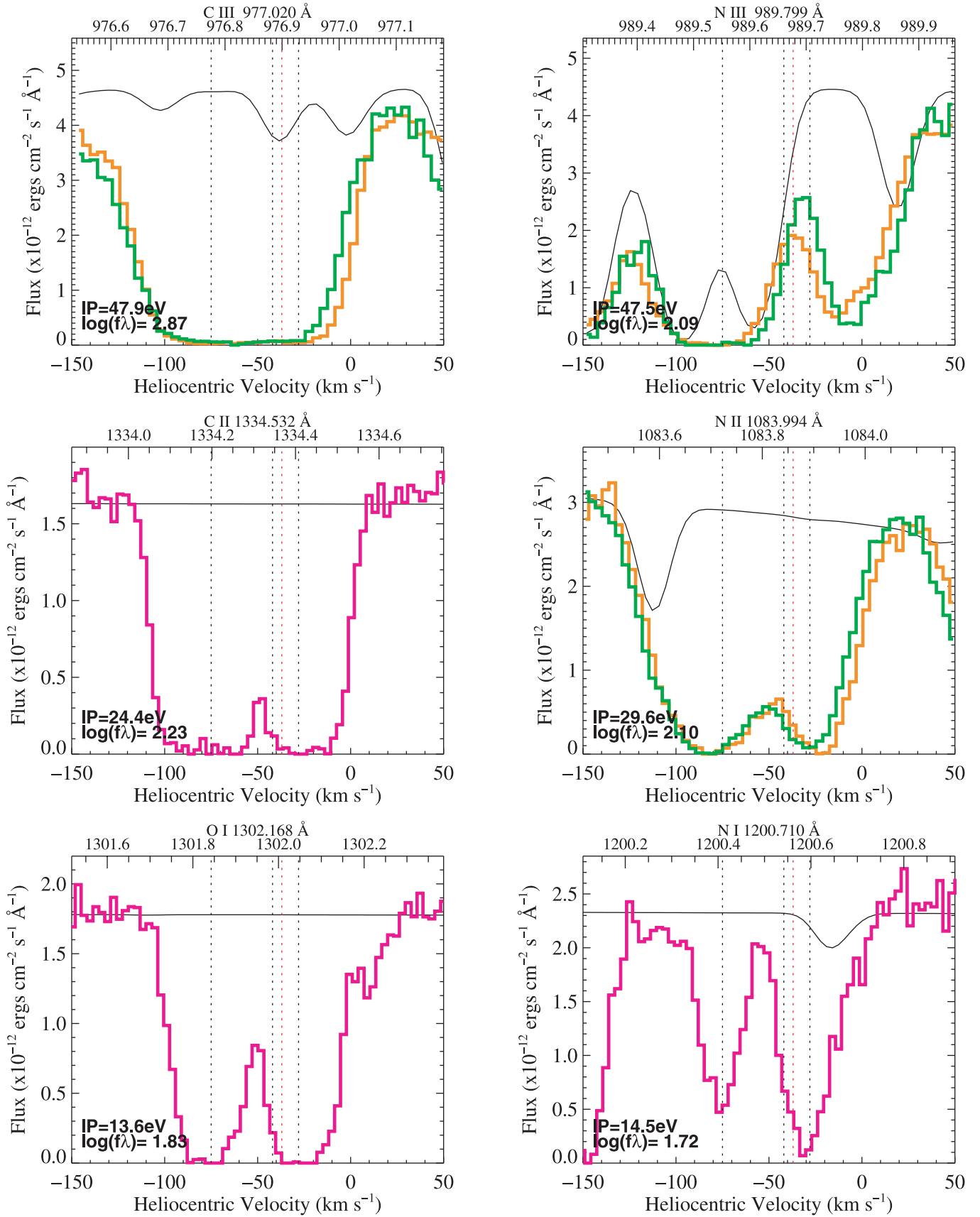


FIG. 16.— Absorption as a function of velocity for representative C III, C II, O I, N III, N II, and N I lines. Ions are fully saturated throughout the nebular flow region blueward of -42 km s^{-1} . Neutrals are less so and favor strong absorption near -75 km s^{-1} . See Fig. 14 for a description of the colors.

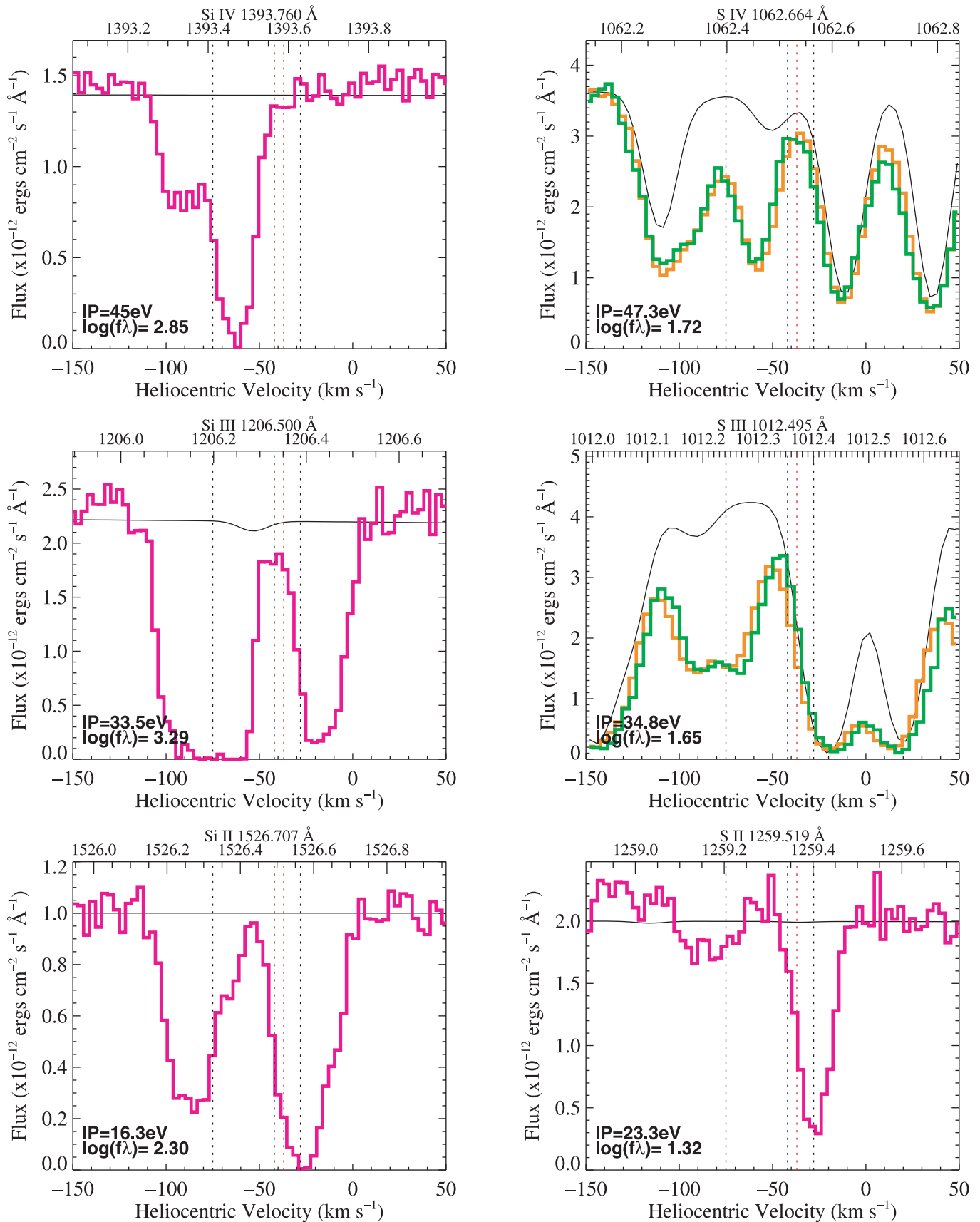


FIG. 17.— Comparison of Si IV–II to S IV–II. The low-ionization species, Si II and S II, dominate in the zone between -75 and -110 km s^{-1} while the high-ionization species, Si IV and S IV, dominate near -60 km s^{-1} . Transition in ionization occurs where absorption by the neutrals and H_2 is strongest. See Fig. 14 for a description of the colors.

along with the absence of any signs of a high-velocity radiation-driven wind, are a challenge to interpret in the context of the simple interacting-winds model of PN formation (Kwok et al. 1978). Meaburn (2005) and Meaburn et al. (2005a, 2005b), who used high-resolution position-and-velocity spectroscopy of the optical emission lines to derive the ionization kinematics of several objects, have arrived at a similar conclusion. They find that ballistic ejection could have been more important than interacting winds in shaping the dynamics of PNe. Balick & Frank (2002) have reviewed in detail some of the more sophisticated thinking about the dynamical processes that shape PNe.

5. Analysis of the C I multiplet fine-structure populations gives better agreement with the expected temperature of ~ 2000 K for collisions with protons and electrons as opposed to collisions with neutrals or molecules. This suggests the molecular and neutral transition component is in close contact with ionized material.

6. The upper limits to CO in the diffuse line-of-sight gas range over $8 \times 10^{13} \text{ cm}^{-2} < N(\text{CO}) < 4 \times 10^{14} \text{ cm}^{-2}$ depending on the assumed CO rotational excitation temperature. The high column density of C I found in the nebula is consistent with it being a daughter product of CO dissociation.

7. The lower limit to the neutral to H₂ column density ratio is $N(\text{H I})/N(\text{H}_2) = 127$ in the transition region (using component number 3 in Table 1).

We will now discuss the constraints imposed by these findings on the ionization kinematics, mass structures, nebular dust, and excitation, formation, and destruction of H₂ within the nebula.

5.1. Ionization Kinematics

Low-mass to intermediate-mass stars begin to evolve into AGB stars when core nucleosynthesis ceases and a degenerate core forms. The AGB phase lasts $\approx 250,000$ years and is marked by a series of high-mass-loss events that merge to produce a slow wind. At some point the star collapses into a hot compact degenerate object. In the PN formation scenario suggested by Kwok et al. (1978) a fast ($\sim 1000 \text{ km s}^{-1}$), low-density, radiation-driven wind from the hot star shocks and ionizes the slow-moving ($\sim 10 \text{ km s}^{-1}$), high-density, mostly molecular AGB wind, resulting in the expanding structures we see at later times.

Natta & Hollenbach (1998) have computed detailed time-dependent changes in the atomic and molecular emissions in a phenomenologically motivated interacting-winds model. Their model consists of an interior ionization region bounded by a shell propagating outward with a velocity of 25 km s^{-1} overrunning and shocking a mostly molecular AGB wind with a velocity of 8 km s^{-1} . An ionization-bounded time-dependent PDR results with three layers. These are a fast-moving ionized shock interface, an adjacent dissociation layer, and a slow-moving molecular layer further downstream. They find most of the shell mass to be vibrationally excited H₂, and H I production to be modest. After ≈ 4000 years they find the infrared H₂ line diagnostic of $S(1)(1-0)/S(1)(2-1)$ indicates a switch from thermal excitation to fluorescent excitation. They also find that H₂ does not co-exist with CO, as dissociation favors $\text{C}^+ + \text{O}$. Consequently, they suggest that molecular masses calculated for old PNe based on CO emission and standard CO/H₂ ratios may be underestimated.

M27 has a kinematic age of $\approx 10,000$ years (O'Dell et al. 2003), so perhaps it is reasonable that the nebula we see today bears little resemblance to this simple layered, two-velocity interacting wind picture. We see no evidence for a shell of predominantly molecular material along the diffuse line-of-sight medium, nor do we see neutral or molecular material at low expansion velocity, as would be expected for an unperturbed AGB wind. The

upper limit to the molecular fraction⁹ in the neutral velocity component expanding at 33 km s^{-1} is $f_{\text{H}_2} = 0.016$, assuming $N(\text{H}) = N(\text{H I})$. We do see evidence for velocity structure in the intermediate ionization states (Figs. 16–17) and H I (Table 1) out to expansion velocities of $\approx 65 \text{ km s}^{-1}$, but there is no evidence of P Cygni profiles with $\sim 1000 \text{ km s}^{-1}$ terminal velocities in any of the high-ionization lines (Fig. 15).

We find instead a rather permuted velocity structure of neutral and molecular material embedded (in velocity space) between the high- and low-ionization mediums. Our findings suggest that the AGB wind has been accelerated through interaction with the hot star and that much of the original mostly molecular atmosphere has been almost completely dissociated. The surviving molecular material is currently interacting strongly with the highly ionized medium, and we postulate that the intermediate ionization species are created and accelerated in this interaction.

Villaver et al. (2002b) have treated the radiative hydrodynamic problem with great rigor for a range of progenitor masses, using as a starting point for their PN simulation the structure found at end of AGB evolution by Villaver et al. (2002a). They find a main nebular shell surrounded by a relatively unperturbed halo. They give detailed figures for the evolution of density, velocity, and H α emission brightness. We note that the amplitude of the velocity structures for their 1–2.5 M_{\odot} models are in the range of the outflow velocities exhibited by the line profiles in Figures 15–17. Unfortunately they give no details on the ionization kinematics of the main and halo regions as a function of time, as Natta & Hollenbach (1998) have done. A model combining the detailed time-dependent calculation of the atomic and molecular emissions of Natta & Hollenbach (1998) with the radiative hydrodynamic rigor of Villaver et al. (2002b) would be useful for interpreting these observations.

5.2. Mass Structures

Identifying kinematic components appearing in spectra with spatial structures in images must be approached with care. The computed total mass of these velocity components will depend on the assumed diameter and thickness of particular structures in the nebula. However, it seems reasonable to expect the 33 km s^{-1} transition zone, where most of the molecular and much of the neutral hydrogen appears, to be at or near the region where the H α brightness drops to near zero. Inside this zone we expect the medium to be completely ionized. The minor axis of the bright H α in M27 is $\approx 300''$ and the full diameter including the faint halo detected by Papamastorakis et al. (1993) is $1025''$. Assuming a distance of 466 pc gives radii for the transition region and the total nebular extent to be ≈ 0.34 and 1.16 pc , respectively. These radii agree reasonably well with the bright H α emitting region and the full extent of the AGB wind found in the Villaver et al. (2002a, 2002b) simulations after $\approx 10,000$ years.

We estimate the masses of the various structures given the following (gross) assumptions. Let the ionized region be a sphere with a radius of 0.34 pc and an electron density of $\sim 300 \pm 200 \text{ cm}^{-3}$ (Barker 1984). The ionized mass becomes $0.4 M_{\odot} \lesssim M_{\text{ion}} \lesssim 1.9 M_{\odot}$. If the total neutral hydrogen column density ($3 \times 10^{19} \text{ cm}^{-2}$) is uniformly distributed in a shell between 0.34 and 1.16 pc with a mean density of 12 cm^{-3} , then $M_{\text{sh}} = 1.7 M_{\odot}$. Our constraint on the progenitor mass, the sum of the ionized, shell, and degenerate-star masses, is $2.6 M_{\odot} \lesssim M_{\text{pro}} \lesssim 4.2 M_{\odot}$.

⁹ By nucleon number $f_{\text{H}_2} \equiv 2N(\text{H}_2)/[2N(\text{H}_2) + N(\text{H})]$ with $N(\text{H}) = N(\text{H I}) + N(\text{H II})$.

By comparison, the molecular material in the diffuse nebular medium has a much lower mass. Although the H_2 is associated with only one neutral hydrogen velocity component, we assume it is spread uniformly throughout the 0.82 pc thick shell. Using this maximal volume yields an upper limit on the molecular mass in the diffuse medium, $M_{\text{dmol}} \lesssim (1.7 M_{\odot})/375 = 4 \times 10^{-3} M_{\odot}$. Meaburn & Lopez (1993) have estimated the total mass of the 11 largest globules, which appear as dark knots against the bright nebular O III emission, to be $M_{\text{omol}} = 1.1 \times 10^{-3} M_{\odot}$. They used measurements of O III transmission and assumed the general ISM gas-to-dust ratio (Bohlin et al. 1978). The Meaburn et al. clump mass estimates compare reasonably well to those of Huggins et al. (1996), who estimate the total molecular mass associated with the CO emitting clumps to be $M_{\text{cmol}} = 2.5 \times 10^{-3} M_{\odot}$. They assumed a thin-ring geometry and a fraction of $\text{CO}/\text{H}_2 = 3 \times 10^{-4}$, a value ≥ 10 times than the highest found by Burgh et al. (2007) for the diffuse ISM. Use of a lower ratio will increase the CO clump mass estimate, as noted by Natta & Hollenbach (1998).

Our upper limit to the diffuse molecular mass is on the same order as the clump mass estimates. The upper limit on the total molecular mass in the nebula, the sum of the diffuse and CO derived masses (assuming the high CO/H_2 ratio), is $M_{\text{mol}} = 6.5 \times 10^{-3} M_{\odot}$. We conclude that there is no large mass of molecular material in M27, either in the diffuse or clumped medium. This is in contrast to the Meixner et al. (2005) finding for the Helix, for which they estimate the mass of all the H_2 emitting globules to be $\sim 0.35 M_{\odot}$. We note that all of the molecular mass estimates for M27 are on the order of the mass of the planets in our own solar system, $\approx 1.3 \times 10^{-3} M_{\odot}$. The suggestion that dense circumstellar bodies have survived the AGB phase and may constitute a significant fraction of the molecular material in the nebula environment cannot be ruled out.

The absence of CO absorption in the diffuse medium is consistent with the Natta & Hollenbach (1998) finding that CO and H_2 are unlikely to coexist in the gas phase, because CO is quickly dissociated after leaving the vicinity of the clumps. Huggins et al. (2002) confirmed this picture with exquisite observations of the globules of the Helix. They show how CO survives only in the shadows of the clumps. The heads of these globules show strong coincident emission of $\text{H}_2 S(1) (1-0)$ and $\text{H}\alpha$, and weaker coincident emission in the shadowed zone. O'Dell et al. (2003) note the globules in M27 tend toward a more irregular and tail-less appearance than those in the Helix. Nevertheless the observation of H_2 emission in the vicinity of the globules suggests they may be a source of H_2 for the diffuse nebular medium.

The temperature of the diffuse medium inferred from the molecular hydrogen rovibration levels exceeds the sublimation temperature of refractory dust, ~ 1500 K (Glassgold 1996). While it is unlikely that the gas and dust will be in thermodynamic equilibrium, the absence of any significant reddening of the CS SED suggests that the diffuse environment is as inhospitable to dust as it is to CO and H_2 . Dust, or perhaps even compact bodies, may exist in the CO-rich dense clumps, which we will argue in § 5.3.2 are the likely source of H_2 for the diffuse medium.

5.3. Constraints on the Excitation, Formation, and Destruction of H_2

5.3.1. H_2 Excitation Processes

The models of Natta & Hollenbach (1998) suggest that in the latter stages of planetary nebula evolution the H_2 is being excited via far-UV continuum fluorescence, yet we have failed to detect this emission. We briefly review this process.

H_2 is excited from the ground vibrational level of $X^1\Sigma_g^+$ into higher electronic states, predominately $B^1\Sigma_u^+$ and $C^1\Pi_u$ (the Lyman and Werner bands), by the absorption of a far-UV photon ($912 \text{ \AA} \leq \lambda \leq 1120 \text{ \AA}$) emitted by a star. The short-wavelength cutoff is imposed by the usual assumption that enough neutral hydrogen is present to shield H_2 from excitation by stellar Lyman continuum photons. The rate of molecular excitation is proportional to the stellar flux absorbed by the rovibrational population of the ground electronic state $X^1\Sigma_g^+$. Fluorescence follows excitation, producing a highly structured emission in the 912–1650 \AA bandpass, as electrons fall back into the excited vibrational levels of $X^1\Sigma_g^+$. Approximately 11%–15% of the time, the fluorescent pumping process leaves the molecule in the vibrational continuum of the ground state ($X^1\Sigma_g^+$), located 4.48 eV above the $(J'', v'') = (0, 0)$ level,¹⁰ resulting in its spontaneous dissociation into $\text{H}(1s) + \text{H}(1s)$ (Stecher & Williams 1967; Dalgarno & Stephens 1970; Draine & Bertoldi 1996). Electrons ending up below the vibrational continuum cascade toward the ground vibrational state $v'' = 0$ via slow quadrupole transitions with radiative lifetimes \sim a few days and longer (Wolniewicz et al. 1998), producing the infrared fluorescence spectrum (Black & Dalgarno 1976).

Lyman and Werner band absorption of the CS continuum unavoidably results in ultraviolet fluorescence, so why was it not detected? To answer this question we estimate the total brightness by simply calculating how many stellar photons are absorbed by H_2 at a given distance, which we take to be the transition zone, and re-emitted into 4π steradians. This will give an upper limit to the total brightness of the H_2 in the diffuse medium. We will neglect absorption by dust.

Using our hydrogen absorption model we find that 30% of the photon flux in the 912–1120 \AA bandpass is absorbed. Reradiation into 4π steradians at 0.34 pc yields a total brightness of $3.4 \times 10^{-5} \text{ ergs cm}^{-2} \text{ s}^{-1} \text{ sr}^{-1}$ (assuming an average energy per photon of $1.6 \times 10^{-11} \text{ ergs}$). Neglecting the fluorescence redistribution into specific lines, and averaging over a 910–1660 \AA bandpass, we find an upper limit to the mean brightness of the continuum fluorescence of $1.1 \times 10^{-18} \text{ ergs cm}^{-2} \text{ s}^{-1} \text{ \AA}^{-1} \text{ arcsec}^{-2}$. This is a factor of ~ 50 below the background estimate shown in Figure 3. So we find that the continuum fluorescence is not very bright and shows no sign of contributing to the ground-state rovibrational population, as there is little in the way of absorption arising from vibrational levels $v'' > 2$. This is in contrast to the strong indication of continuum fluorescence found in the reflection nebula NGC 2023 by Meyer et al. (2001), where they observed absorption lines from all $v'' \leq 14$ states of $X^1\Sigma_g^+$ in a STIS spectrum of the central star HD 37903.

The low levels of continuum fluorescence found here are consistent with the infrared spectroscopic diagnostics presented by Zuckerman & Gatley (1988), who found the ratio of $S(1) (1-0) / S(1) (2-1)$ (at 2.122 and 2.248 μm , respectively) to be ≈ 10 , placing it in the thermal regime well above the value of 2 expected from fluorescence (Black & Dalgarno 1976). If the $S(1) (1-0)$ line were produced by fluorescence, then the $10^{-4} \text{ ergs cm}^{-2} \text{ s}^{-1} \text{ sr}^{-1}$ measured by Zuckerman & Gatley (1988) would imply a total ultraviolet brightness ~ 850 times this value (in energy units; 50 times in photon units) and would have easily been detected by the rocket experiment.

The detection of $\text{Ly}\alpha$ fluorescence pumped through two resonant transitions in the $v'' = 2$ vibrational level of the $X^1\Sigma_g^+$ electronic state [$R(6) (1-2)$ at 1215.730 \AA and $P(5) (1-2)$ at 1216.073] reported recently by Lupu et al. (2006) serves to

¹⁰ Direct radiative dissociation of the $X^1\Sigma_g^+$ state is dipole forbidden.

emphasize that in a radiation-bounded nebula two-thirds of the Lyman continuum photons emitted by the star are converted to Ly α photons (Spitzer 1998). The contrast between the Ly α and continuum fluorescence is enhanced in our case, because the number of Lyman continuum photons exceeds the number of photons in the 912–1120 Å bandpass by a factor of 15.¹¹ Even so, modeling by Lupu et al. (2006) shows the Ly α fluorescence rate is too low to cause detectable deviations in a thermalized ground-state population at a temperature of 2000 K. We conclude that the observed rovibration population distribution of the hot H₂ is dominated by collisional processes. The deviations from a pure thermal distribution will be addressed in § 5.4.

5.3.2. Molecular Hydrogen Formation and Destruction

The observed neutral atomic-to-molecular hydrogen ratio [$N(\text{H I})/N(\text{H}_2) = 127$] can be used to constrain formation and destruction processes in the diffuse nebular medium using the formula

$$\frac{dn_2}{dt} = F - Dn_2. \quad (2)$$

Here F is the sum over all formation processes, D is the sum over all destruction processes, and n_2 is the density of H₂. We will not attempt to provide a comprehensive listing of all the processes; rather we will make some limiting assumptions to develop the constraints.

In the limit where formation is absent ($F = 0$) the solution for $n_2(t)$ is an exponential with an e -folding time equal to D^{-1} . If we assume the destruction process is radiative dissociation, then $D = \chi p_{\text{diss}} \zeta_{\text{pump}}$, where p_{diss} is the mean dissociation fraction, ζ_{pump} is the mean probability per second of an upward radiative transition, and χ the standard interstellar radiation field multiplier. Draine & Bertoldi (1996) have conveniently tabulated ζ_{pump} and p_{diss} for a number of transitions for $\chi = 1$, neglecting self-shielding. They find fairly narrow ranges for ζ_{pump} and p_{diss} , and weighted mean values of these products over the H₂ ground-state rovibrational distribution are relatively insensitive to the actual distribution for our purposes here. We will use $p_{\text{diss}} = 0.15$ and $\zeta_{\text{pump}} = 3.5 \times 10^{-10} \text{ s}^{-1}$, yielding $D_1 = 5.3 \times 10^{-11} \text{ s}^{-1}$ as a representative dissociation rate for $\chi = 1$.

To compute χ we use the Rauch model, which has a total photon luminosity of $1.2 \times 10^{45} \text{ photons s}^{-1}$ in the 912–1120 Å bandpass at the stellar surface. At 0.34 pc, the photon flux is $8.9 \times 10^7 \text{ photons cm}^{-2} \text{ s}^{-1}$, yielding a rather modest scale factor of $\chi = 7.4$ relative to the average ISM background of $1.2 \times 10^7 \text{ photons cm}^{-2} \text{ s}^{-1}$ (Draine & Bertoldi 1996). The resulting e -folding time for radiative dissociation is 21 years, and it would only take 100 years for the $N(\text{H I})/N(\text{H}_2)$ ratio to reach its currently observed level. We conclude the source term for the diffuse medium $F \neq 0$; i.e., the H₂ in the diffuse medium must be constantly replenished.

We now turn to the equilibrium limit, i.e., $dn_2/dt = 0$. The formation term is $F = \gamma n_1$, where the neutral hydrogen density is n_1 . We consider formation of H₂ either by dust or by associative detachment $\text{H} + \text{H}^- \rightarrow \text{H}_2 + e^-$. In the former case $\gamma_d = 3 \times 10^{-17} \text{ cm}^3 \text{ s}^{-1}$ (Natta & Hollenbach 1998) and n is the gas density. In the latter case n is the electron density n_e and γ_- is given

by equation (15) of Natta & Hollenbach (1998). The rate coefficient γ_- depends explicitly on hydrogen ionization fraction and temperature. At $T = 2000 \text{ K}$ we find $\gamma_- \approx \gamma_d$ when the ionization fraction $x_+ \equiv n_+/n_1 = 0.5$. When $x_+ = 0.05$, $\gamma_- \approx 15\gamma_d$.

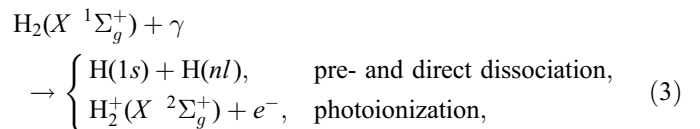
Equating formation and destruction we solve for the total density n required for formation to keep pace with dissociation. With $\chi = 7.4$ the dissociation rate is $D = 3.9 \times 10^{-10} \text{ s}^{-1}$ and we find $n = (D/\gamma)(n_2/n_1) = 10^5 \text{ cm}^{-3}$ for the dust and the $x_+ = 0.5$ cases. For $x_+ = 0.05$ the density is $\approx 7000 \text{ cm}^{-3}$. These densities are consistent with the Meaburn & Lopez (1993) clump estimates for M27, but they are much higher than the gas and electron densities we found from the C I analysis in § 4.4.2 for the transition zone or the electron density given by Barker (1984) for the ionized region.

We conclude that the density in the diffuse medium is not high enough to support formation of H₂ either on dust grains or through the associative detachment processes and that the most likely source of excited H₂ is from photoevaporating clumps (see Huggins et al. 2002; López-Martín et al. 2001). Whether the clumps are reservoirs of H₂ that formed long ago or are currently active in forming H₂ by these processes is an open question. The transport process that moves molecular hydrogen out of the clumpy medium and constantly replenishes the diffuse medium is a dynamical process, which results in the exposure of H₂ to Lyman continuum radiation.

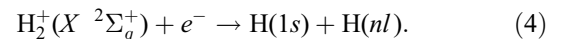
5.4. Beyond Spontaneous Dissociation: Lyman Continuum Dissociation and Photoionization of H₂

We have two outstanding puzzles. One is the apparent “two temperature” slope in the rovibration population (Fig. 9). The other is the excess H α /H β ratio in the absence of any significant stellar or nebular reddening. We speculate here that a confluence of environmental factors—molecular hydrogen interacting and excited by a ionized medium that is optically thin to Lyman continuum radiation—conspire to contribute to the production of H α emission at a few percent of the radiative recombination rate and to create the two-temperature slope.

We know that while the energies of thermal electrons in the nebula are high enough to populate the $X^1\Sigma_g^+$ vibrational levels above $v'' > 0$, they are not nearly high enough to lead to dissociative excitation. For that a radiative process is required such that $\text{H}_2(X^1\Sigma_g^+) + \gamma$ ultimately results in $\text{H}(1s) + \text{H}(3p)$, which can then branch into Ly β or H α + Ly α . Stecher & Williams (1967) discussed two possible radiative paths that lead to the dissociation of H₂. In § 5.3.1 we described the familiar spontaneous dissociation process that leads to $\text{H}(1s) + \text{H}(1s)$ following excitation into the Lyman ($B^1\Sigma_u^+$) and Werner ($C^1\Pi_u$) bands. The other path (with multiple channels) is



with $n \geq 2$ and $l = s, p, d, \dots$ the angular momentum of the excited atom. The photoionization channel can further undergo dissociative recombination with low-energy electrons,



These channels are not usually considered to be important for H I regions (PDRs) because the photoionization, predissociation, and direct-dissociation processes all have thresholds above the

¹¹ Additional enhancement of Ly α fluorescence results from the concentration of excitations into a single $v' = 1$ level of the $B^1\Sigma_u^+$ state, as opposed to the continuum case where excitations to a multitude of vibrational levels, $0 \leq v' \leq 20$ for $B^1\Sigma_u^+$ and $0 \leq v' \leq 6$ for $C^1\Pi_u$, compete for a relatively smaller number of photons.

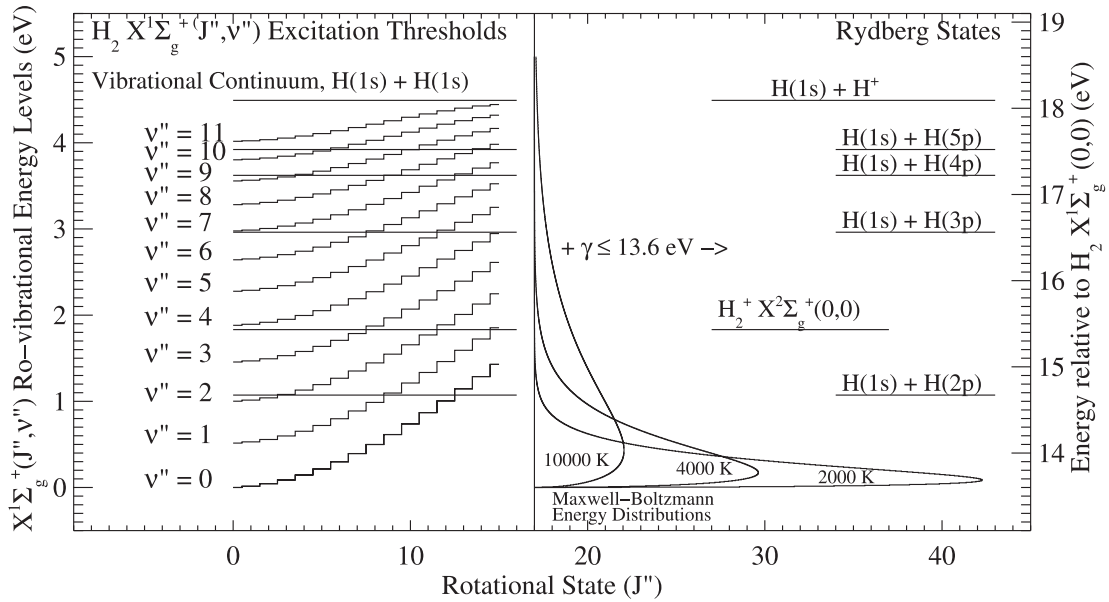


FIG. 18.—Energy-level diagram illustrating the threshold energy rovibration levels (J'' , v'') that can be excited to Rydberg orbitals [$H(1s) + H(nl)$, $2 \leq n \leq \infty$, $l = s, p, d, \dots$] with photon energies ≤ 13.6 eV. The threshold for excitation into the H_2^+ cation ground state is also shown. Normalized Maxwell-Boltzmann energy distributions for $T = 10,000, 4000$, and 2000 K show schematically the relative change in the energy-level population as a function of temperature.

Lyman limit. In such an instance the H_2 is usually cold and optically thick neutral hydrogen shields the H_2 from dissociation (Spitzer 1948). However, for H_2 in H II regions it is not at all clear that this assumption is justified. At the interface of a mostly molecular clump embedded in an ionized medium, as we encounter in M27, there will be a zone where the H I and H_2 are optically thin to ionizing radiation and the H_2 is excited (hot). In this case the ionization and dissociation of H_2 by photons with energies above the Lyman limit at 13.598 eV should also be considered.

Direct-dissociation paths proceed through excited rovibrational levels in the $B^1\Sigma_u^+$, $B'^1\Sigma_u^+$, and $C^1\Pi_u$ upper electronic states of H_2 , while the $B''^1\Sigma_u^+$, $D^1\Pi_u$, $D'^1\Pi_u$, and $D''^1\Pi_u$ states can undergo predissociation as well as direct dissociation. The experimental distinction is that a predissociation process shows structure (in the absorption cross sections as a function of wavelength) while direct dissociation does not (Lee & Judge 1976). The structure is a consequence of the perturbative coupling with the dissociative continuum of the overlapping excited electronic states.

The vibrational continua of the upper electronic states converge into Rydberg orbitals, which are essentially $n \geq 2$ principal quantum number electrons in orbit around the cation (H_2^+) core. At asymptotic nuclear separation these orbitals become free $H(1s) + H(nl)$. Transitions between $X^1\Sigma_g^+$ and its own vibrational continuum [$H(1s) + H(1s)$] at 4.48 eV can proceed only by quadrupole radiation, while transitions between $X^1\Sigma_g^+$ and the upper singlet electronic states are dipole allowed. The vibrational continua of $B^1\Sigma_u^+$, $B'^1\Sigma_u^+$, and $C^1\Pi_u$ converge to $H(1s) + H(2l)$ at 14.67 eV (844.8 Å); $D^1\Pi_u$ and $B''^1\Sigma_u^+$ converge to $H(1s) + H(3l)$ at 16.56 eV (748.46 Å); $D'^1\Pi_u$ converges to $H(1s) + H(4l)$ at 17.22 eV (719.74 Å); and $D''^1\Pi_u$ converges to $H(1s) + H(5l)$ at 17.52 eV (707.175 Å), measured with respect to $(J'', v'') = (0, 0)$ of $H_2(X^1\Sigma_g^+)$. The onset of photoionization ($H_2 + \gamma \rightarrow H_2^+ + e^-$) is at 15.43 eV (803.7 Å) in between the $H(1s) + H(2l)$ and $H(1s) + H(3l)$. The right side of Figure 18 shows the energy levels of Rydberg states in relation to the cation ground state.

Glass-Maujean et al. (1986) give cross sections for the photoexcitation of Ly α [$H(1s) + H(2l)$] from the direct dissociation and predissociation of $H_2(X^1\Sigma_g^+)$. The total cross section peaks at the threshold (14.67 eV), reaching 5×10^{-18} cm², and falls monotonically thereafter. Cook & Metzger (1964) have shown the detailed structure in the H_2 photodissociation and ionization cross section from 550 to 1000 Å. The photoionization cross section peaks near 18 eV at $\approx 10^{-17}$ cm². Some of the discrete dissociation peaks to the red are \approx a factor of 3 higher at a resolution limit of 0.5 Å. Flannery et al. (1977) have calculated and tabulated cross sections for excitation out of vibrationally excited states of $H_2(X^1\Sigma_g^+, v'') + \gamma \rightarrow H_2^+(X^2\Sigma_g^+, v') + e^-$ as a function of wavelength, assuming $\Delta J = 0$.

Yan et al. (1998) produced a piecewise continuous function for the photoionization cross section valid over the interval $300 \text{ eV} \geq E_{\text{ph}} \geq 15.4 \text{ eV}$. At high frequencies the cross section for H_2 ionization is 2.8 times that for H I. Above 18.09 eV H_2 can undergo dissociative ionization, $H_2 + \gamma \rightarrow H + H^+ + e^-$, or even $H^+ + H^+ + 2e^-$, but the branching ratios into these channels are small over the wavelengths of Lyman continuum emitted by the CS (see Yan et al. 1998 and references therein), where the yield for dissociative recombination should be $p_{\text{dr}} \approx 1$.

Stecher & Williams (1967) have noted how the thresholds for transition into the upper-level continua are lower for excited rovibrational (J'' , v'') levels of $X^1\Sigma_g^+$. Cook & Metzger (1964) observed this effect in the redward broadening of the dissociation thresholds by ≈ 14 Å in their experiments conducted at room temperature. It is actually possible to dissociate and photoionize H_2 with photon energies less than the Lyman limit, for a high enough rovibrational level (J'' , v''). We quantify this in Figure 18, where the energies of the rovibrational levels in the $X^1\Sigma_g^+$ state in relation to the asymptotically free states are shown. Horizontal lines drawn through the (v'' , J'') energy levels indicate the thresholds for excitation with photons ≤ 13.6 eV in energy. Maxwell-Boltzmann energy distributions with temperatures of 2000, 4000, and 10,000 K are drawn to indicate schematically how the relative populations of the upper levels change as a function of T .

Rotational states above $J'' = 13$ in $v'' = 0$, $J'' = 9$ in $v'' = 1$, and $J'' = 3$ in $v'' = 2$ can be excited to $H(1s) + H(2p)$ by photons with energies ≤ 13.6 eV. The steepening of the slope of the level population in Figure 9 might result from a radiative depopulation of the higher J'' states into the asymptotic $H(1s) + H(2p)$ state. The populations of the upper levels become selectively depleted, a process we refer to as “radiative skimming.” However, the slope change in the $v'' = 0, 1$ curves are observed to occur at $J'' \approx 6, 8$ respectively, which are smaller than given above. We take this as evidence for skimming by Lyman continuum photons.

We also see from Figure 18 that the creation of $H(1s) + H(3p)$ without the benefit of Lyman continuum photons would require extremely high temperatures ≥ 4000 K. The two-step process $H_2(X^1\Sigma_g^+) + \gamma \rightarrow H_2^+(X^2\Sigma_g^+) + e^- \rightarrow H(1s) + H(3p)$ is energetically more accessible than the direct $H_2(X^1\Sigma_g^+) + \gamma \rightarrow H(1s) + H(3p)$. Observations by Lee & Judge (1976) of the direct production of Balmer series fluorescence from H_2 by direct dissociation and predissociation support this conjecture. They find the dissociation yield with respect to total dissociation + photoionization cross section to be on the order of a few percent. For example, at 716 Å the cross section for production of $H\alpha$ was 0.23×10^{-18} cm², which is about a factor of 40 lower than for the production of H_2^+ .

H_2^+ is also homonuclear (Leach & Moss 1995), so radiative transitions among the 18 vibrational levels of the $X^2\Sigma_g^+$ ground state are not dipole allowed. The vibrational continuum of $H_2^+(X^2\Sigma_g^+)[H^+ + H(1s)]$ is only 2.646 eV above the $(J'', v'') = (0, 0)$ ground state, so electron energy need not be high to produce dissociative recombination into the overlapping Rydberg states. Excitation to higher bound states ($2^2\Sigma_g^+$, $2^2\Pi_u$) have poor overlap integrals (Franck–Condon factors), yielding small branching ratios to these dipole-allowed upper levels. Once created, H_2^+ will undergo rapid dissociative recombination with free electrons, $H_2^+ + e^- \rightarrow H(1s) + H(nl)$, producing a fluorescent cascade of Lyman and Balmer emission. The amount of $H\alpha$ and $Ly\alpha$ produced will depend on the vibrational distribution in the cation energy levels and the electron impact energies.

Takagi (2002) has shown in detail how the dissociative recombination cross sections of the individual $H(nl)$ channels depends strongly on the vibrational level of the $H_2^+ X^2\Sigma_g^+(v'')$ state. The cross sections are generally highest for e^- collisions with the lowest energies and fall in proportion to the inverse of the electron energy. Typical values near zero electron energy range from 10^{-15} to 10^{-17} cm², ignoring rotation. Including the rotational state introduces resonances and can strongly modulate the cross sections at low electron energies. Schneider et al. (1994) have calculated total dissociative recombination rates for H_2^+ for hydrogen plasmas with temperatures between 20 and 4000 K for individual rovibrational states of H_2^+ , but they provide no estimate of the branching ratios into the individual $H(1s) + H(nl)$ final states.

5.5. Optically Thin Photoionization Destruction of H_2

We have suggested that photoionization by Lyman continuum photons of excited H_2 in an optically thin medium ultimately results in a fluorescent cascade of Lyman and Balmer emission. Verification of this hypothesis will require exploring the detailed balance of hydrogen ions, atoms, and molecules in the recombination regime between case A (the optically thin limit where Lyman series emissions are not reabsorbed in the nebula) and case B (the optically thick limit where Lyman series emissions are reabsorbed on the spot).

In the previous section we have given references to the necessary molecular cross sections for computing the photoionization rates out of the vibrationally excited molecule and into the

excited cation (Flannery et al. 1977), along with the cross sections for electron impact dissociation of excited cation states into the Rydberg manifold (Takagi 2002). The calculation of the Lyman and Balmer series emissivity resulting from the two-step process of molecular photoionization followed by dissociative recombination goes beyond the scope of this paper.

Here we show an example of the competitiveness of photoionization with spontaneous dissociation for the destruction of H_2 in the optically thin limit. The ionization rates at the transition zone (0.34 pc) for H_2 and $H\text{ I}$ were calculated by integrating the cross sections for these species, using Yan et al. (1998) for H_2 and Spitzer (1998, eq. [5-4]) for $H\text{ I}$, over the SED of our stellar model from $\lambda < 911.7$ Å according to Spitzer (1998, eq. [4-36]). We do not include contributions from direct-dissociation and predissociation processes, which are likely to be substantial for excited H_2 , so our dissociation estimate will be conservative. We find $\zeta_{H_2 \rightarrow H_2^+} = 3.4 \times 10^{-9}$ s⁻¹ compared to $\zeta_{H \rightarrow H^+} = 1.4 \times 10^{-9}$ s⁻¹. The ratio is 2.4, so we conclude that in the optically thin limit it is easier to ionize the hydrogen molecule than the atom.

In an optically thin medium at the inferred radius of the transition zone the molecular photoionization rate $\zeta_{H_2 \rightarrow H_2^+}$ exceeds the far-UV pump rate $\chi\zeta_{\text{pump}}$ (§ 5.3.2) by a factor of 1.3. If we assume that the yield for dissociative recombination [$H_2^+ + e^- \rightarrow H(1s) + H(nl)$] following creation of the cation is 100%, then the photoionization mediated dissociation of H_2 can be expected to be $p_{\text{dr}}\zeta_{H_2 \rightarrow H_2^+} / (p_{\text{diss}}\chi\zeta_{\text{pump}}) \approx 9$ times the spontaneous dissociation. This process increases the rate required for the clumps to resupply the diffuse medium with H_2 in the steady state limit. We note that Natta & Hollenbach (1998) do not include Lyman continuum dissociation of H_2 in their model. This may be why they find the shell mass is dominated by H_2 as opposed our finding that $N(H\text{ I})/N(H_2) \gg 1$.

6. CONCLUSIONS AND SUGGESTIONS FOR FUTURE INVESTIGATIONS

M27 is an excellent laboratory for testing theories of formation, excitation, and destruction of molecules and dust, because the stellar temperature, mass, and gravity, as well as the nebular distance, masses, abundances, and excitation states, are well quantified.

We find that the diffuse nebular medium is generally inhospitable to molecules and dust. The diffuse H_2 accounts for a small fraction ($\sim 0.3\%$) of the total nebular mass. H_2 is easily destroyed by the stellar radiation field in the diffuse medium on a timescale ~ 20 years. A steady state abundance requires a source, most likely the clumpy medium. If the clump density is high enough, it may support molecular hydrogen formation via dust or mediated by radiative detachment, although we cannot rule out photoevaporation of relic material.

The finding of neutrals and molecules at a transition velocity between slow-high and fast-low ionization material suggests that collisional interaction with charged particles is the most important process for establishing the observed rovibration level populations in molecular hydrogen. Lupu et al. (2006) find that the rate of $Ly\alpha$ pumping is not high enough to change the level population of a thermal distribution, and we find that the rate of continuum-pumped fluorescence is even lower. However, if the neutral hydrogen is optically thin in the transition zone, then stellar Lyman continuum can radiatively skim the upper rotational states of $v'' = 0, 1$ and create the apparent break in the high- and low-temperature slopes at the observed levels, but this is likely to be a second-order process.

Dissociation and ionization of the hydrogen molecule by Lyman continuum photons can also lead to the production of

Lyman and Balmer series emission and may provide an explanation for the excess $H\alpha/H\beta$ ratio observed in the apparent absence of extinction by dust. In the optically thin limit Lyman continuum mediated destruction rates can exceed by an order of magnitude the spontaneous dissociation rate and should be considered when calculating the equilibrium abundance of excited H_2 in H II regions.

At this late stage in the evolution of M27 most of the original AGB atmosphere has been dissociated and accelerated to velocities in excess of 33 km s^{-1} but not above 68 km s^{-1} . A high-speed radiation-driven stellar wind is not detected in the present epoch. The mechanism for acceleration remains unidentified.

The analysis of the formation and destruction of H_2 rests in part on the determination of the H I velocity structures identified in the Dwingeloo survey data to guide the column density determination carried out with the STIS and *FUSE* data. However, our conclusions regarding the overall abundance of molecular hydrogen with respect to H I and the need for a molecular source for the diffuse medium are immune to changes in the atomic abundance by factors of 10. Nevertheless it would be prudent to check the velocity structure found here with a high-resolution mapping using a telescope with a smaller beam ($\approx 4'$). It appears that the velocity separation of M27 permits discrimination with respect to the Galactic H I background. This and a reasonable signal strength have allowed the apparent detection of H I in a PN where only upper limits have existed previously (Schneider et al. 1987).

Our lowest bound for $N(\text{CO})/N(\text{H}_2) < 10^{-3}$ in the diffuse nebular medium is a factor of 30 higher than ratio used by Huggins et al. (1996) to constrain the CO clump mass. Should an *HST* servicing mission 4 be successful in resurrecting STIS, then higher signal-to-noise data could be acquired to examine the $N(\text{CO})/N(\text{H}_2)$ more carefully, using a number of rovibrational bands. It should be possible to place limits on $\log N(\text{CO}) \lesssim 13$ (e.g., Burgh et al. 2007).

We emphasize that our analysis applies to the direct line of sight gas, the diffuse nebular medium, which we find to be dust free. The existence of clumps with column densities of CO in excess of 10^{16} cm^{-2} immediately adjacent to regions with CO column densities $\lesssim 10^{14} \text{ cm}^{-2}$ attests to the steep density gradients within the nebular environment and the probable low covering fraction of the densest clumpy medium. The clumps may well be reservoirs of material depleted from the diffuse medium. Measuring the abundance of metals on either side of the neutral transition velocity could provide information on whether photoevaporation of the globules is an important process for the enrichment of metals in the high-velocity zone (McCandliss &

Kruk 2007). In addition, infrared spectral and imaging observations with *Spitzer* could tell us much more about the prevalence of dust and molecules elsewhere in the nebula. Mapping of the nebular Balmer emission line ratios with respect to the $H_2 S(1) (2-1) / S(1) (1-0)$ emission ratio would be especially useful for further exploring the connections between H_2 production of Balmer emission and the prevalence of thermal or fluorescence processes in the clumpy medium.

During the review of this paper, work by O'Dell et al. (2007) was brought to our attention. O'Dell et al. derive the total flux in the infrared H_2 emission lines in the Helix Nebula and argue that only Lyman continuum radiation from the star has enough power to sustain the H_2 IR emission at the observed levels. They also propose that charge exchange between H_2 and O^+ could be a significant dissociation channel. Future work examining the efficiency of their proposed charge exchange mechanism for mediating the dissociation of H_2 in comparison to the Lyman continuum dissociation process proposed here would be a useful addition to the nascent field of Lyman continuum dominated PDRs.

We are grateful to Patrick J. Huggins, who suggested that the molecular hydrogen kinematics might share similarities with CO and providing encouragement to complete this work. We acknowledge the sounding rocket mission operation teams from Wallops Flight Facility and the Physical Science Laboratory operated by New Mexico State University and located at the White Sands Missile Range. The coordination of observing specialists Jack Dembicky, Russet McMillan, and Gabrelle Saurage at APO allowed for the efficient execution of an ambitious observing program. This work is based on observations made with the NASA-CNES-CSA *Far Ultraviolet Spectroscopic Explorer*. *FUSE* is operated for NASA by the Johns Hopkins University under NASA contract NAS5-32985. Observations were also obtained with the Apache Point Observatory 3.5 m telescope, which is owned and operated by the Astrophysical Research Consortium. In addition, some of the data presented in this paper were obtained from the Multimission Archive at the Space Telescope Science Institute (MAST). STScI is operated by the Association of Universities for Research in Astronomy, Inc., under NASA contract NAS5-26555. Support for MAST for non-*HST* data is provided by the NASA Office of Space Science via grant NAG5-7584 and by other grants and contracts.

Facilities: FUSE, HST, IUE

REFERENCES

- Abgrall, H., Roueff, E., Launay, F., Roncin, J. Y., & Subtil, J. L. 1993a, *A&AS*, 101, 273
 ———. 1993b, *A&AS*, 101, 323
 Aleman, I., & Gruenwald, R. 2004, *ApJ*, 607, 865
 Bachiller, R., Cox, P., Josselin, E., Huggins, P. J., Forveille, T., Miville-Deschênes, M. A., & Boulanger, F. 2000, in *ISO Beyond the Peaks: Proc. 2nd ISO Workshop on Analytical Spectroscopy* (ESA SP-456; Noordwijk: ESA), 171
 Balick, B., & Frank, A. 2002, *ARA&A*, 40, 439
 Barker, T. 1984, *ApJ*, 284, 589
 Benedict, G. F., et al. 2003, *AJ*, 126, 2549
 Black, J. H., & Dalgarno, A. 1976, *ApJ*, 203, 132
 Bohlin, R. C., Dickinson, M. E., & Calzetti, D. 2001, *AJ*, 122, 2118
 Bohlin, R. C., Savage, B. D., & Drake, J. F. 1978, *ApJ*, 224, 132
 Brocklehurst, M. 1971, *MNRAS*, 153, 471
 Burgh, E. B., France, K., & McCandliss, S. R. 2007, *ApJ*, 658, 446
 Burgh, E. B., McCandliss, S. R., & Feldman, P. D. 2002, *ApJ*, 575, 240
 Burgh, E. B., McCandliss, S. R., Pelton, R., France, K., & Feldman, P. D. 2001, *Proc. SPIE*, 4498, 296
 Burnham, R. 1978, *Burnham's Celestial Handbook: An Observer's Guide to the Universe beyond the Solar System* (rev. ed.; New York: Dover)
 Cahn, J. H. 1976, *AJ*, 81, 407
 Cahn, J. H., Kaler, J. B., & Stanghellini, L. 1992, *A&AS*, 94, 399
 Capriotti, E. R. 1973, *ApJ*, 179, 495
 Cardelli, J. A., Clayton, G. C., & Mathis, J. S. 1989, *ApJ*, 345, 245
 Ciardullo, R., Bond, H. E., Sipior, M. S., Fullton, L. K., Zhang, C.-Y., & Schaefer, K. G. 1999, *AJ*, 118, 488
 Cook, G. R., & Metzger, P. H. 1964, *J. Opt. Soc. Am.*, 54, 968
 Cox, P., et al. 1998, *ApJ*, 495, L23
 Dalgarno, A., & Stephens, T. L. 1970, *ApJ*, 160, L107
 Dinerstein, H. L., Sterling, N. C., & Bowers, C. W. 2006, in *ASP Conf. Ser.* 348, *Astrophysics in the Far-Ultraviolet: Five Years of Discovery with FUSE*, ed. G. Sonneborn, H. Moos, and B-G Andersson (San Francisco: ASP), 328
 Draine, B. T., & Bertoldi, F. 1996, *ApJ*, 468, 269
 Dyson, J. E., Hartquist, T. W., Pettini, M., & Smith, L. J. 1989, *MNRAS*, 241, 625
 Flannery, M. R., Tai, H., & Albritton, D. L. 1977, *At. Data Nucl. Data Tables*, 20, 563

- France, K., McCandliss, S. R., Burgh, E. B., & Feldman, P. D. 2004, *ApJ*, 616, 257
- Glassgold, A. E. 1996, *ARA&A*, 34, 241
- Glass-Maujean, M., Guyon, P. M., & Breton, J. 1986, *Phys. Rev. A*, 33, 346
- Goudis, C., McMullan, D., Meaburn, J., Tebbutt, N. J., & Terrett, D. L. 1978, *MNRAS*, 182, 13
- Gry, C., Boulanger, F., Nehmé, C., Pineau des Forêts, G., Habart, E., & Falgarone, E. 2002, *A&A*, 391, 675
- Harris, H. C., Dahn, C. C., Monet, D. G., & Pier, J. R. 1997, in *IAU Symp.* 180, *Planetary Nebulae*, ed. H. J. Habing & H. J. G. L. M. Lamers (Dordrecht: Kluwer), 40
- Hartmann, D., & Burton, W. B. 1997, *Atlas of Galactic Neutral Hydrogen* (Cambridge: Cambridge Univ. Press)
- Hawley, S. A., & Miller, J. S. 1978, *PASP*, 90, 39
- Herald, J. E., & Bianchi, L. 2002, *ApJ*, 580, 434
- . 2004, *ApJ*, 611, 294
- Huggins, P. J., Bachiller, R., Cox, P., & Forveille, T. 1996, *A&A*, 315, 284
- Huggins, P. J., Forveille, T., Bachiller, R., Cox, P., Ageorges, N., & Walsh, J. R. 2002, *ApJ*, 573, L55
- Jahn, D., Rauch, T., Reiff, E., Werner, K., Kruk, J. W., & Herwig, F. 2007, *A&A*, 462, 281
- Jenkins, E. B., & Shaya, E. J. 1979, *ApJ*, 231, 55
- Jenkins, E. B., & Tripp, T. M. 2001, *ApJS*, 137, 297
- Kaler, J. B. 1976, *ApJS*, 31, 517
- Kastner, J. H., Weintraub, D. A., Gately, I., Merrill, K. M., & Probst, R. G. 1996, *ApJ*, 462, 777
- Kwok, S., Purton, C. R., & Fitzgerald, P. M. 1978, *ApJ*, 219, L125
- Leach, C. A., & Moss, R. E. 1995, *Annu. Rev. Phys. Chem.*, 46, 55
- Lee, L. C., & Judge, D. L. 1976, *Phys. Rev. A*, 14, 1094
- Livio, M., & Soker, N. 1983, *A&A*, 125, L12
- López-Martín, L., Raga, A. C., Mellema, G., Henney, W. J., & Cantó, J. 2001, *ApJ*, 548, 288
- Lupu, R., France, K., & McCandliss, S. R. 2006, *ApJ*, 644, 981
- Martin, P. G., Keogh, W. J., & Mandy, M. E. 1998, *ApJ*, 499, 793
- McCandliss, S. R. 2001, in *ASP Conf. Ser.* 247, *Spectroscopic Challenges of Photoionized Plasmas*, ed. G. Ferland & D. W. Savin (San Francisco: ASP), 523
- . 2003, *PASP*, 115, 651
- McCandliss, S. R., Burgh, E. B., & Feldman, P. D. 2000, *Proc. SPIE*, 4139, 70
- . 2001, *Appl. Opt.*, 40, 2626
- McCandliss, S. R., & Kruk, J. 2007, *ApJS*, in press
- McCandliss, S. R., Martinez, M. E., Feldman, P. D., Pelton, R., Keski-Kuha, R. A., & Gum, J. S. 1994, *Proc. SPIE*, 2011, 310
- McPhate, J. B., Feldman, P. D., McCandliss, S. R., & Burgh, E. B. 1999, *ApJ*, 521, 920
- Meaburn, J. 2005, preprint (astro-ph/0512099)
- Meaburn, J., Boumis, P., Christopoulou, P. E., Goudis, C. D., Bryce, M., & López, J. A. 2005a, *Rev. Mex. AA*, 41, 109
- Meaburn, J., Boumis, P., López, J. A., Harman, D. J., Bryce, M., Redman, M. P., & Mavromatakis, F. 2005b, *MNRAS*, 360, 963
- Meaburn, J., Christopoulou, P. E., & Goudis, C. D. 1992, *MNRAS*, 256, 97
- Meaburn, J., & Lopez, J. A. 1993, *MNRAS*, 263, 890
- Meixner, M., McCullough, P., Hartman, J., Son, M., & Speck, A. 2005, *AJ*, 130, 1784
- Meyer, D. M., Lauroesch, J. T., Sofia, U. J., Draine, B. T., & Bertoldi, F. 2001, *ApJ*, 553, L59
- Miller, J. S. 1973, *Mem. Soc. R. Sci. Liège*, 5, 57
- Miller, J. S., & Mathews, W. G. 1972, *ApJ*, 172, 593
- Moos, H. W., et al. 2000, *ApJ*, 538, L1
- Morton, D. C. 2003, *ApJS*, 149, 205
- Napiwotzki, R. 1999, *A&A*, 350, 101
- Natta, A., & Hollenbach, D. 1998, *A&A*, 337, 517
- Nussbaumer, H., & Schmutz, W. 1984, *A&A*, 138, 495
- O'Dell, C. R., Balick, B., Hajian, A. R., Henney, W. J., & Burkert, A. 2002, *AJ*, 123, 3329
- . 2003, *Rev. Mex. AA Ser. Conf.*, 15, 29
- O'Dell, C. R., Henney, W. J., & Ferland, G. J. 2007, *AJ*, in press
- Papamastorakis, J., Xilouris, K. M., & Paleologou, E. V. 1993, *A&A*, 279, 536
- Pottasch, S. R., Wesselius, P. R., Wu, C.-C., & van Duinen, R. J. 1977, *A&A*, 54, 435
- Quijano, J. K. 2003, *STIS Instrument Handbook, Version 7.0* (Baltimore: STScI)
- Rauch, T. 2003, *A&A*, 403, 709
- Reay, N. K., & Atherton, P. D. 1985, *MNRAS*, 215, 233
- Redman, M. P., Viti, S., Cau, P., & Williams, D. A. 2003, *MNRAS*, 345, 1291
- Rybicki, K. R., & Denis, C. 2001, *Icarus*, 151, 130
- Sahnou, D. J., et al. 2000, *ApJ*, 538, L7
- Schneider, I. F., Dulieu, O., Giusti-Suzor, A., & Roueff, E. 1994, *ApJ*, 424, 983
- Schneider, S. E., Silverglate, P. R., Altschuler, D. R., & Giovanardi, C. 1987, *ApJ*, 314, 572
- Shull, J. M. 1978, *ApJ*, 219, 877
- Siess, L., & Livio, M. 1999, *MNRAS*, 304, 925
- Soker, N. 1999, *MNRAS*, 306, 806
- Spitzer, L. 1998, *Physical Processes in the Interstellar Medium* (New York: Wiley)
- Spitzer, L. J. 1948, *ApJ*, 107, 6
- Spitzer, L. J., & Cochran, W. D. 1973, *ApJ*, 186, L23
- Spitzer, L. J., & Zweibel, E. G. 1974, *ApJ*, 191, L127
- Stecher, T. P., & Williams, D. A. 1967, *ApJ*, 149, L29
- Sterling, N. C., Dinerstein, H. L., Bowers, C. W., & Redfield, S. 2005, *ApJ*, 625, 368
- Sternberg, A., & Dalgarno, A. 1989, *ApJ*, 338, 197
- Takagi, T. 2002, *Phys. Scr.*, T96, 52
- Traulsen, I., Hoffmann, A. I. D., Rauch, T., Werner, K., Dreizler, S., & Kruk, J. W. 2005, in *ASP Conf. Ser.* 334, *14th European Workshop on White Dwarfs*, ed. D. Koester & S. Moehler (San Francisco: ASP), 325
- Tylenda, R., Acker, A., Raytchev, B., Stenholm, B., & Gleizes, F. 1991, *A&AS*, 89, 77
- van Dishoeck, E. F., & Black, J. H. 1986, *ApJS*, 62, 109
- Villaver, E., García-Segura, G., & Manchado, A. 2002a, *ApJ*, 571, 880
- Villaver, E., Manchado, A., & García-Segura, G. 2002b, *ApJ*, 581, 1204
- Wesson, R., & Liu, X.-W. 2004, *MNRAS*, 351, 1026
- Williams, R. J. R. 1999, *MNRAS*, 310, 789
- Wilson, R. E. 1953, *General Catalogue of Stellar Radial Velocities* (Washington, DC: Carnegie Institution)
- Wolniewicz, L., Simbotin, I., & Dalgarno, A. 1998, *ApJS*, 115, 293
- Yan, M., Sadeghpour, H. R., & Dalgarno, A. 1998, *ApJ*, 496, 1044
- Zuckerman, B., & Gately, I. 1988, *ApJ*, 324, 501